

Exploring the dust content of galactic haloes with *Herschel* III. NGC 891

J. H. Yoon,¹ Crystal L. Martin,¹★ S. Veilleux,^{2,3}★ M. Meléndez,^{2,4} T. Mueller,⁵ K. D. Gordon,⁴ G. Cecil,⁶ J. Bland-Hawthorn¹ and C. Engelbracht⁸

¹Department of Physics, University of California, Santa Barbara, CA 93106, USA

²Department of Astronomy, University of Maryland, College Park, MD 20742, USA

³Joint Space-Science Institute, University of Maryland, College Park, MD 20742, USA

⁴Space Telescope Science Institute, Baltimore, MD 21218, USA

⁵Max-Planck-Institute for Extraterrestrial Physics (MPE), D-85748 Garching, Germany

⁶Department of Physics and Astronomy, University of North Carolina, Chapel Hill, NC 27599, USA

⁷Department of Physics, University of Sydney, Sydney, NSW 2006, Australia

⁸Department of Astronomy, University of Arizona, Tucson, AZ 85721, USA

Accepted 2020 November 9. Received 2020 October 14; in original form 2020 July 3

ABSTRACT

We present deep far-infrared observations of the nearby edge-on galaxy NGC 891 obtained with the *Herschel Space Observatory* and the *Spitzer Space Telescope*. The maps confirm the detection of thermal emission from the inner circumgalactic medium (halo) and spatially resolve a dusty superbubble and a dust spur (filament). The dust temperature of the halo component is lower than that of the disc but increases across a region of diameter ≈ 8.0 kpc extending at least 7.7 kpc vertically from one side of the disc, a region we call a superbubble because of its association with thermal X-ray emission and a minimum in the synchrotron scale height. This outflow is breaking through the thick disc and developing into a galactic wind, which is of particular interest because NGC 891 is not considered a starburst galaxy; the star formation rate surface density, $0.03 \text{ M}_\odot \text{ yr}^{-1} \text{ kpc}^{-2}$, and gas fraction, just 10 per cent in the inner disc, indicate the threshold for wind formation is lower than previous work has suggested. We conclude that the star formation surface density is sufficient for superbubble blowout into the halo, but the cosmic ray electrons may play a critical role in determining whether this outflow develops into a fountain or escapes from the gravitational potential. The high dust-to-gas ratio in the dust spur suggests the material was pulled out of NGC 891 through the collision of a minihalo with the disc of NGC 891. We conclude that NGC 891 offers an example of both feedback and satellite interactions transporting dust into the halo of a typical galaxy.

Key words: galaxies: haloes – galaxies: individual: NGC891 – galaxies: ISM – galaxies: photometry – galaxies: star formation – infrared: galaxies .

1 INTRODUCTION

Studying giant spiral galaxies beyond the Local Group determines whether the assembly of the Milky Way was typical. Having a vantage point outside the system also makes observations of the stellar halo and circumgalactic medium (CGM) easier. The disc component can be completely separated from the halo, for example, when such galaxies are viewed edge-on. The edge-on orientation of the nearby galaxy, NGC 891, is ideal for studying the interaction between the disc, CGM, and satellite galaxies.

NGC 891 resides in a spiral-rich group representative of typical environments and has a luminosity similar to the group's brightest member, NGC 1023. NGC 891 is similar to the Milky Way in spiral type and rotation speed (Swaters, Sancisi & van der Hulst 1997). In both galaxies, a large fraction of the halo stars have been accreted from satellites (Mouhcine, Ibata & Rejkuba 2010; Bell et al. 2008) and recent star formation is elevated (compared to the disc as a whole) in a molecular ring and central circumnuclear disc (Scoville et al. 1993).

The warm ionized gas in the interstellar medium (ISM) of NGC 891 is more extended than the Reynold's (1989) layer in the Milky Way, and the central surface density of the warm ionized medium is roughly twice as high in NGC 891 as in the Milky Way (Rand, Kulkarni & Hester 1990; Dettmar 1990). The molecular gas mass of NGC 891 is 2.5 times larger than that of the Milky Way, and the current star formation rate (SFR) is proportionally higher. Star formation in NGC 891 is more active than in the Milky Way disc yet not high enough to be considered a starburst. The specific SFR and stellar mass of NGC 891 are similar to many Cosmic Origins Spectrograph (COS) Haloes galaxies at redshift $z \approx 0.2$ (Tumlinson et al. 2011; Werk et al. 2014). The proximity of NGC 891, however, has made it possible to directly detect emission from the CGM. The recent 21-cm detection of cold gas out to 90–120 kpc along the minor axis (Das et al. 2020), combined with the X-ray detection of the virialized halo gas (Hodges-Kluck, Bregman & Li 2018) and the well-studied synchrotron halo (Schmidt et al. 2019), together provide excellent observational constraints on the properties of the inner CGM.

The vertical distribution of hot gas (Bregman & Pildis 1994), neutral gas (Swaters et al. 1997), molecular gas (Garcia-Burillo et al. 1992), warm dust (McCormick, Veilleux & Rupke 2013),

* E-mail: cml@ucsb.edu (CLM); veilleux@astro.umd.edu (SV)

and stars (van der Kruit & Searle 1981) have been measured in NGC 891 and found to contain extraplanar components. A full 30 per cent of the H_I resides in a halo (Oosterloo, Fraternali & Sancisi 2007). The thermal emission from the halo dust indicates a larger dust mass than was originally estimated from absorption features (Howk & Savage 1997, 2000; Popescu et al. 2000; Bianchi 2008; Popescu et al. 2011). The first maps of the dust mass and temperature showed a strong correlation with the distribution of stellar mass and star formation, respectively (Hughes et al. 2014). The X-ray halo of NGC 891 was the first detected in a non-starburst galaxy, but it has remained controversial as to whether the hot gas was heated by galactic accretion (Hodges-Kluck & Bregman 2012) or feedback processes (Strickland et al. 2004a, b; Tüllmann et al. 2006).

The presence of cold dust in NGC 891 has been known for several decades, but little was known about its spatial distribution due to the low resolution of the far-infrared (FIR) and submm observations. Observations of NGC 891 with *Spitzer*/MIPS (Multiband-Imaging Photometer for *Spitzer*) resolved disc and halo components at 24 μm but lacked the spatial resolution at longer wavelengths required to map the spectral energy distribution, hereafter the SED (GO-20528, PI: C. Martin). As part of the Very Nearby Galaxies Survey, a *Herschel* Guaranteed Time Key Project, the large vertical extent of the dust in NGC 891 was resolved with *Herschel* PACS (Photodetector Array Camera and Spectrometer)/SPIRE (Spectral and Photometric Imaging Receiver) (Hughes et al. 2014).

In this paper, we combine deeper *Herschel* observations (OT1_sveilleu_2, PI: S. Veilleux) with the *Spitzer*/MIPS data to better describe the amount of halo dust and its origin. This work builds on our examination of NGC 4631 (Meléndez et al. 2015, hereafter Paper I), a lower mass galaxy with a higher SFR surface density (SFRSD, Tüllmann et al. 2006), and six nearby dwarf galaxies including NGC 1569 (McCormick et al. 2018, hereafter Paper II). The interstellar dust in NGC 891 plays an important role in its appearance. Young, star-forming regions, for example, are much more apparent along the north-east (approaching) side of the disc compared to the receding (south-west) half due to the accumulation of dust along the inner edges of the trailing spiral arms. Our deep observations directly show the relative importance of stellar feedback and satellite interactions for building a dusty halo. This new perspective should prove generally valuable for understanding the dust-to-gas ratio in galaxy haloes (Ménard & Fukugita 2012), and the processes taking place in the outskirts of galaxies in general (Veilleux et al. 2020).

Our presentation is structured as follows. In Section 2, we present the FIR/submm observations. The morphological components of the dust distribution are defined in Section 3 before describing our fits to the multiband photometry and the resulting physical properties in Section 4. In Section 5, we argue that the superbubble will become a galactic wind and discuss the origin of a puzzling, extraplanar dust spur. Our conclusions are briefly summarized in Section 6.

We adopt a distance of 9.77 Mpc (Ferrarese et al. 2000), which is the weighted mean of distances derived from *Hubble Space Telescope* observations of planetary nebula and surface brightness fluctuations. This distance gives an angular scale of 47.37 pc arcsec⁻¹.

2 OBSERVATION AND DATA REDUCTION

2.1 *Spitzer*/IRAC and *Spitzer*/MIPS data

Spitzer images at 3.6, 4.5, and 24 μm are used in this study. Images taken with the Infrared Array Camera (IRAC) at 3.6 and 4.5 μm

cover the entire galaxy (PID: 3, PI: G. Fazio). The observations consist of a series of dithered images taken with exposure times from 0.4 to 96.80 s. The basic calibrated data were obtained from the *Spitzer* archive and combined into a mosaic using the MONTAGE package (<http://montage.ipac.caltech.edu/>) correcting for variations in the overall level and rejecting outliers. The point source flux accuracy is \sim 2 per cent (Reach et al. 2005) and the extended source surface brightness accuracy is estimated at \sim 4 per cent.

We observed NGC 891 with the MIPS (Rieke et al. 2004) at 24 μm (PID: 20528, PI: C. Martin). The images were obtained using the medium rate, scan-map mode and the scan legs of 0.5° with 148 arcsec cross-scan offsets. This observation consists of 5 scans (Obs ID 14815488, 14815744, 14816000, 14816256, and 14816512) with total exposure times of 1600 s. The data were reduced with the MIPS Data Analysis Tool v3.04 (DAT Gordon et al. 2005). Extra steps were carried out to improve the images including readout offset correction, array-averaged background subtraction (using a low-order polynomial fit to each leg, with the region including NGC 891 excluded from this fit), and exclusion of the first five images in each scan leg due to boost frame transients. The point source flux accuracy is \sim 2 per cent (Engelbracht et al. 2007) and the extended source surface brightness accuracy is estimated at \sim 4 per cent.

The 24 μm image resolves stars and background galaxies, which we mask out for accurate photometry of the galaxy. We identified background galaxies using SExtractor. Briefly, we set the detection threshold to 1.5σ in surface brightness. The sources identified by the segmentation map were then replaced by the values in the background map at the same locations.

2.2 *Herschel*/PACS and *Herschel*/SPIRE data

The PACS (Poglitsch et al. 2010) observation for NGC 891 was conducted as our cycle 1 open-time program (OT1_sveilleu_2, PI: S. Veilleux). This program utilizes PACS blue 70 μm and red 160 μm channels with six scan position angles at 55°, 70°, 85°, 95°, 110°, and 125° (Obs IDs: 1342237999, 1342238000, 1342238001, 1342238002, 1342238003, and 1342238004). The exposure time per each scan was 5596 s (total 9.3 h) including overhead. The scan map leg length and separation were 4 arcmin and 4 arcsec and the number of scan map legs was 60. Each scan map was repeated three times for redundancy reasons.

We also retrieved, reduced, and analysed the PACS data from *The Herschel EDGE-on galaxy Survey* (HEDGES, Murphy 2011, OT2_emurph01_3) for the analysis of extended structure as these data have a larger field of view than do our observations. For the blue channel (70 μm), the scan angle was 45° and 135° with an exposure time of 6550 s. The scan map leg length and separation were 14.6 arcmin and 14.0 arcsec and the number of scan map legs was 70. For the green channel (100 μm), the exposure time was 8977 s at scan angles of 45° and 135°. The scan map leg length and separation were 14.6 arcmin and 20.0 arcsec and the number of scan map legs was 51.

The observation in 250, 350, and 500 μm bands were performed using the SPIRE (Griffin et al. 2010) onboard *Herschel Space Observatory*. Our SPIRE images are the part of the KINGFISH open-time key program, KPGT_cwils01_1, from *Herschel* guaranteed time key project, *Physical Processes in the Interstellar Medium of Very Nearby Galaxies*¹ (ID: 1342189430, Griffin et al. 2010). The beam sizes are 465.39, 822.58, and 1768.66 arcsec² at 250, 350, and

¹<http://hedam.lam.fr/VNGS/index.php>

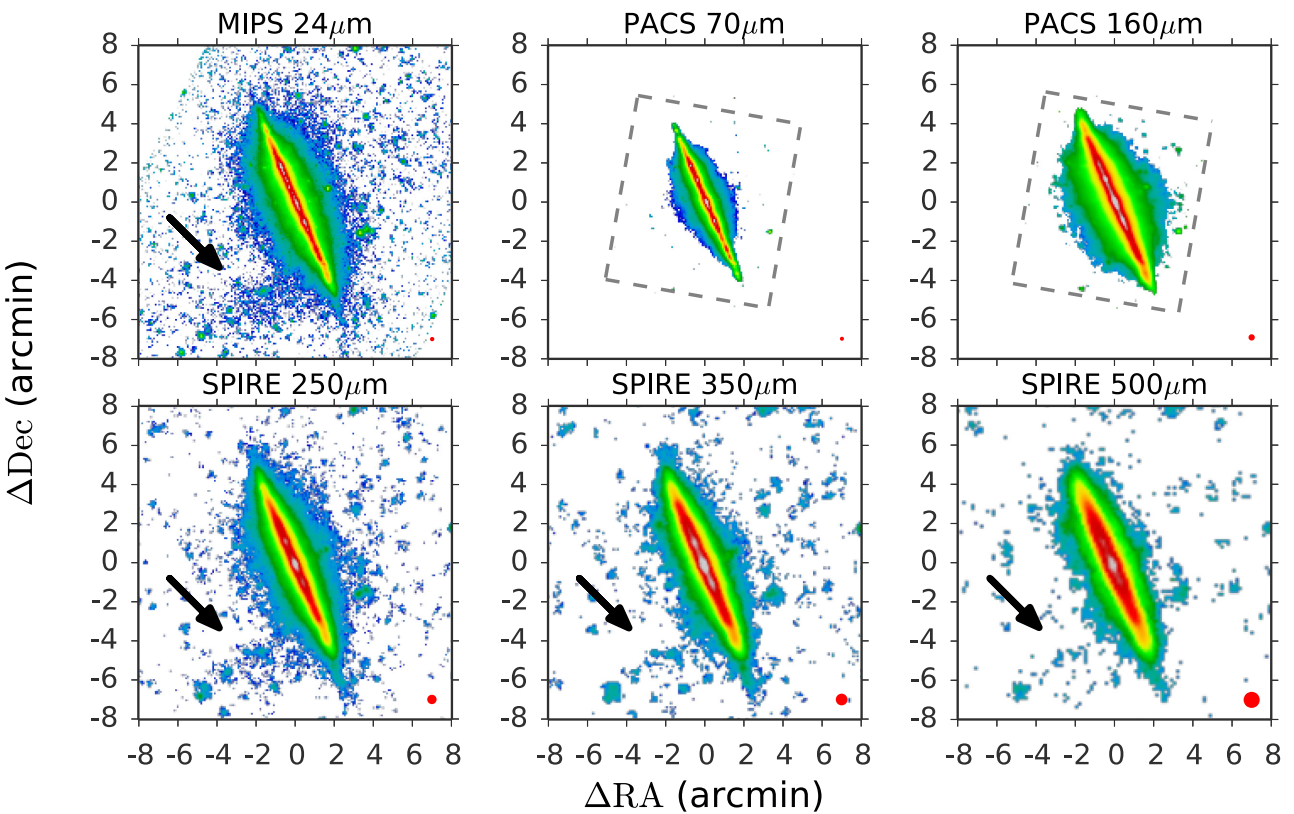


Figure 1. *Spitzer* MIPS 24 μm , *Herschel* PACS 70 and 160 μm , and *Herschel* SPIRE 250, 350, and 500 μm images of NGC 891. The colour bars show surface brightness on a logarithmic scale; the maximum central surface brightness is white, and the images are greyed out below an S/N ratio of 1.5. The black arrow indicates the dust spur to the south-east. The red circles indicate the size of the PSF. The colour bar ranges (in Janskys per pixel on a logarithmic scale) are as follows: 0.0032–63 (24 μm), 10^{-5} to 0.079 (70 μm), 10^{-5} –0.40 (160 μm), 10^{-4} to 0.50 (250 μm), 10^{-4} –0.25 (350 μm), and 10^{-4} to 0.16 (500 μm).

500 μm , respectively (SPIRE Data Reduction Guide, Table 6.7) and the exposure times were 1678 s for each channel.

2.3 Data reduction

For the PACS data, we used the *Herschel* Interactive Processing Environment (HIPE, Ott 2010) version 10.0 for data reduction. This reduction procedure contains the extraction of the calibration tree for the data processing, electronic crosstalk correction, flat-fielding, and unit conversion from volts to Janskys per pixel. The final map was created with the algorithm implemented in *Scanamorphos* (v24.0, Roussel 2013). The error and weight maps were also produced with *Scanamorphos* and the error map is defined as the error on the mean brightness in each pixel.

The SPIRE data were processed from level 0 up to level 1 with HIPE scripts in the *Scanamorphos* distribution. The same steps as PACS processing were conducted. The thermal drifts are subtracted by using the smoothed series of thermistors located on the detector array as the input of the drift model (see Ott 2010 for details). A more detailed description of the data reduction can be found in Paper I.

Both sets of PACS observations contain a low-amplitude artefact parallel to the major axis on the eastern side of the disc mid-plane. It is 70 arcsec away to the south-east and the flux in the ghosts is less than 0.5 per cent of the corresponding object flux. This region immediately east of the disc mid-plane was not used in our analysis of the vertical structure of the disc. The amplitude of the feature is small enough, that it has a negligible effect on our integrated flux measurements.

Table 1. Properties of NGC 891.

Property	Value
RA (J2000) ^a	2:22:33.0
Dec. (J2000) ^a	42:20:53
d (Mpc) ^b	9.77
V_{circ} (km s $^{-1}$) ^c	225
SFR (M_{\odot} yr $^{-1}$)	5.0
$F_{\nu}^{24\mu\text{m}}$ (Jy)	6.2 ± 0.6
$F_{\nu}^{70\mu\text{m}}$ (Jy)	100 ± 10
$F_{\nu}^{160\mu\text{m}}$ (Jy)	334 ± 33
$F_{\nu}^{250\mu\text{m}}$ (Jy)	167 ± 17
$F_{\nu}^{350\mu\text{m}}$ (Jy)	72 ± 7
$F_{\nu}^{500\mu\text{m}}$ (Jy)	26 ± 3

Notes: ^aCoordinates of the maximum intensity in the 4.5 μm IRAC image.

^bDistance from Ferrarese et al. (2000).

^cRotation speed from Swaters et al. (1997).

2.4 Integrated photometry of NGC 891 and global properties

Fig. 1 compares the new (24, 70, and 160 μm) images to the SPIRE images at 250, 350, and 500 μm . We define the centre of NGC 891 by the location of the maximum 4.5 μm IRAC intensity, a proxy for the centre of the stellar bulge. In Fig. 1 and subsequent images, the coordinates (0,0) reference this position. Table 1 provides the corresponding sky coordinates.

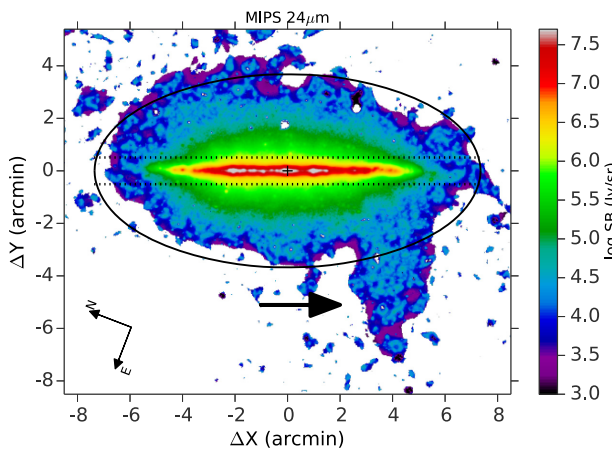


Figure 2. *Spitzer*/MIPS 24 μm image for NGC 891 adaptively smoothed after subtraction of background sources. The colour scale for the surface brightness is logarithmic. The scale height and scale length of the stars are indicated by the rectangle, ± 0.5 arcmin (1.4 kpc) by ± 7.35 arcmin (20.9 kpc) (Ibata, Mouhcine & Rejkuba 2009). The extended emission forms a halo which we define by an ellipse (semimajor axis of 7.35 arcmin and semiminor axis of 3.68 arcmin, or 10.5 kpc). An arrow indicates the dust spur.

We measured fluxes from the 24, 70, 160, 250, 350, and 500 μm images. In order to match the point spread function (PSF), we convolved the images with the kernels provided by Aniano et al. (2011). The image pixel scale and coordinates were then matched using the IDL code `hrebin.pro` and `hastrom.pro` in the GODDARD package. These processes conserve total image flux.

The aperture adopted for the integrated photometry is based on a growth curve measured from photometry of the SPIRE 500 μm image in increasingly larger apertures. It is an elliptical aperture of semimajor axis of 7.35 arcmin and semiminor axis of 3.68 arcmin that includes most of the dust emission seen in 24 μm image after convolution to the PSF of the 500 μm image. Fig. 2 shows this aperture on the 24 μm image.

Within an annulus at larger radii, we masked point sources and background galaxies based on the morphology in the 24 μm data. The sky background was taken as the mean data value following 2σ clipping. The variance in this region was used to compute the standard deviation of the mean. This uncertainty on the mean background dominates the total background error for large apertures. We also include a term for the pixel-to-pixel statistical variance in the background.

The error budget is dominated by the calibration uncertainties, which exceed the uncertainties from both background subtraction and photon noise. Following Paper I, we conservatively estimate the background error at 10 per cent in all bands.

We computed colour corrections for the PACS and SPIRE fluxes assuming a blackbody spectrum modified by the dust emissivity, $\kappa_v = \kappa_0 (v/v_0)^\beta$ with $\beta = 2$, and a blackbody temperature of $T = 30$ K.² We divided the original flux measurements by the following correction factors: 0.977, 1.037, 0.9796, 0.9697, and 0.9796 for, respectively, 70, 160, 250, 350, and 500 μm . The estimated aperture corrections

²As the PACS and SPIRE pipelines compute fluxes assuming a monochromatic spectrum, we applied a colour correction. See Section 4.3 in ‘PACS Photometer Passbands and Color Correction Factors for Various Source SEDs’, PICC-ME-TN-038, version 1.0, and table 5.7 in SPIRE Handbook, HERSCHEL-DOC-0798, version 2.5.

were small compared to the photometric errors and were therefore not applied.

The integrated fluxes listed in Table 1 for the 24, 70, 160, 250, 350, and 500 μm bands. Our measurements agree with both Bendo, Galliano & Madden (2012) and Hughes et al. (2014) to within the 1σ errors.

3 MORPHOLOGICAL FEATURES OF THE WARM DUST IN NGC 891

The 24 μm image in Fig. 2 resolves several structures contributing to the thermal emission. The brightest of these are thin and thick dust components aligned with the centre of the galaxy, components we will refer to as the dusty disc and dusty halo, respectively. Modelling these components in the longer wavelength *Herschel* images is sensitive to how the PSF is modelled (Bocchio et al. 2016).

We adopt the scale heights that Bocchio et al. (2016) fitted to the vertical surface brightness profiles. Fig. 2 of their paper shows that the shape of the vertical surface brightness profile requires a two-component fit. The thin, unresolved dust component significantly reduces the scale height of the fitted thick dust component. A consequence of this interplay is that the thick dust component has the largest 24 μm scale height above the region of the stellar disc where the thin dust component is faintest. Based on the vertical profile perpendicular to a region of the disc with low star formation activity, Bocchio et al. (2016) conclude that the scale height of the dusty halo is $h_z = 1.36 \pm 0.01$ kpc. The scale height of the dusty halo is therefore comparable to that of the thick stellar disc, whose size we have indicated in Fig. 2.

Our analysis describes two non-axisymmetric components of the FIR morphology: (1) the large filament marked by the arrow in Fig. 2, and (2) a dusty superbubble erupting from the centre of the galaxy. The superbubble was detected previously at X-ray energies (Hodges-Kluck & Bregman 2012; Hodges-Kluck et al. 2018), and we present the first description of its dust content. The filament, or *dust spur*, is a new discovery enabled by the spatial resolution and sensitivity of the new observations.

3.1 The dust spur

The arrow in Fig. 2 indicates a filament of 24 μm emission extending 6.90 arcsec (19.6 kpc) south-east of the dust halo. We discovered this filament in the *Spitzer* MIPS data and confirmed it using *Herschel*. Fig. 1 shows the SPIRE detections. The structure is outside the field of view of our new PACS images, so we examined the PACS images obtained previously by The HEDGES (Murphy 2011) and found a clear detection at 160 μm , a few clumps of emission at 100 μm , and weaker emission at 70 μm . The FIR filament is therefore not an instrumental artefact.

We looked for a background cluster of galaxies at this location but found none in either X-ray images or optical images.³ Our photometry indicates a broad SED, which we show is consistent with thermal dust emission in Section 4. The FIR filament may therefore be a component of the dusty halo of NGC 891, and we will refer to this morphological feature as *the dust spur*. Spectroscopy of an emission line would confirm its association with NGC 891; alternatively, higher resolution mapping would be useful to definitively rule out an unresolved galaxy cluster.

³The $z = 0.0184$ cluster Abell 347 lies to the south-east at 02:25:50.9, +41:52:30 (NED).

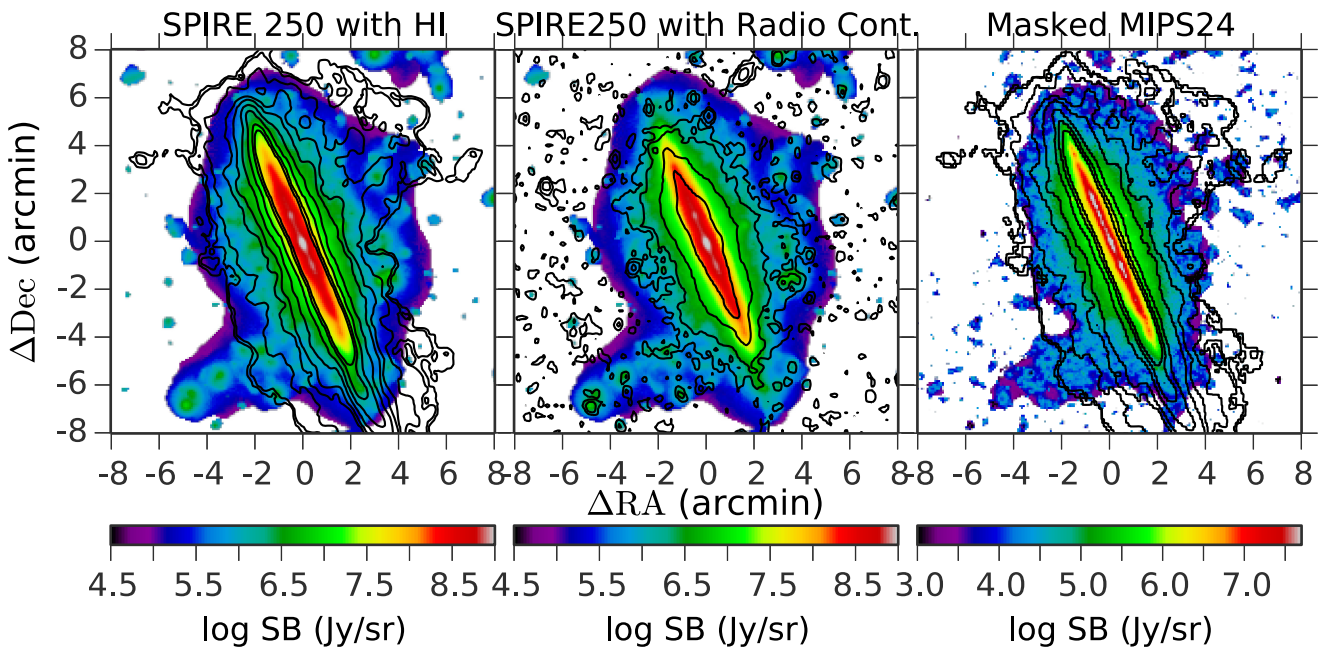


Figure 3. Adaptively smoothed maps. We applied ADAPTSMOOTH (Zibetti 2009) with a minimum $S/N = 5 \text{ pixel}^{-1}$. Left: the *Herschel* 250 μm map overlaid with the H I emission contours from Oosterloo et al. (2007). The contour levels for H I emission are 0.01, 0.03, 0.08, 0.16, 0.47, 0.78, 1.56, 3.11, 6.23, and $9.34 \times 10^{21} \text{ cm}^{-2}$. Middle: the *Herschel* 250 μm map overlaid with the radio continuum contours from Oosterloo et al. (2007). The contour levels for the radio continuum are 0.1, 0.4, 2, and 10 mJy beam $^{-1}$. Right: the *Spitzer* 24 μm map with the H I contours. The discrete sources in the background were masked prior to the smoothing.

The morphology of the dust spur shows no connection to the centre of the galaxy, making an association with a galactic outflow unlikely. When projected on the sky, the long axis of the dust spur is roughly perpendicular to the disc. The filament emerges at a galactocentric radius $R = 4.0 \text{ arcmin}$ (11 kpc) and extends 6.9 arcmin (19.6 kpc) to the south-east, and has a width of $\sim 2.0 \text{ arcmin}$ (6 kpc).

The dust spur is *not* coincident with the large filament of neutral hydrogen described by Oosterloo et al. (2007, see also Pingel et al. 2018). In Fig. 3, we show their H I 21-cm emission contours on the *Herschel* and *Spitzer* images. The lowest contour at $N(\text{H}\text{I}) = 1 \times 10^{19} \text{ cm}^{-2}$ extends 22 kpc north-west of NGC 891. The dust spur extends to the south-east, in contrast, and is not visible in the H I contours. We will show that the H I filament and the dust spur have different compositions in Section 4.

The middle panel of Fig. 3 compares the dust emission to the radio continuum. The overall shape of the radio continuum contours is similar to the distribution of FIR emission, whereas the H I contours show a lower ratio of vertical height to galactocentric radius.

A close inspection of the dust spur suggests a spatial coincidence between the brightest emission regions at 250 μm and the local maxima in the faintest radio continuum contours. This correlation should be interpreted cautiously. Unresolved sources in the SPIRE map could be background sources unrelated to NGC 891, and the radio detections have low signal-to-noise ratio (S/N). If the radio sources are at the redshift of the dust spur, then the radio flux levels of the clumps, 0.2 mJy beam $^{-1}$, combined with the fluxes listed in Table 3, are consistent with FIR–radio relation defined by star-forming regions (Yun, Reddy & Condon 2001; Bell 2003). These data raise the possibility that the dust spur is a region of active star formation.

3.2 The superbubble

We smoothed the 70 μm image to match the resolution of the 160 μm image, and then we divided the smoothed 70 μm image by the 160 μm image to produce a colour map from the PACS data. This colour map resolves a broad plume of thermal dust emission, indicated by the arrow in Fig. 4. This structure emerges from a region of the disc within roughly 1.8 arcmin (5.1 kpc) of the nucleus, slightly inside the 3.1 arcmin radius of the molecular ring. It extends north-west, roughly perpendicular to the disc, reaching a height of 2.7 arcmin (7.7 kpc). We refer to this structure as *the superbubble* but will argue in Section 5 that a galactic wind is actually developing here. We will show that this region has a slightly higher dust temperature than the surrounding halo in Section 4.

Contours of the soft X-ray emission (Hodges-Kluck & Bregman 2012) outline the perimeter of the dusty superbubble. In deeper X-ray observations, this hot ($kT = 0.71 \pm 0.01 \text{ keV}$) gas is concentrated near the most active region of star formation and co-exists with gas near the virial temperature, $kT = 0.20 \pm 0.01 \text{ keV}$ (Hodges-Kluck et al. 2018). Harder diffuse X-ray emission is detected within 5 kpc of the galactic centre; its physical origin remains unclear.

The soft X-ray emission from galactic winds is produced mostly at the interface between the hot wind and a cooler component of the multiphase outflow (Strickland et al. 2004a, b). The smaller panels in Fig. 4 overlay the radio continuum contours and the H α contours on the PACS colour map. The H α image shows one prominent filament extending well into the dusty bubble, but the H α image is not sensitive enough to determine the amount of correlation with the superbubble morphology at other wavelengths. We have shown in Fig. 3 that the radio contours closely follow the morphology of the dusty halo. As

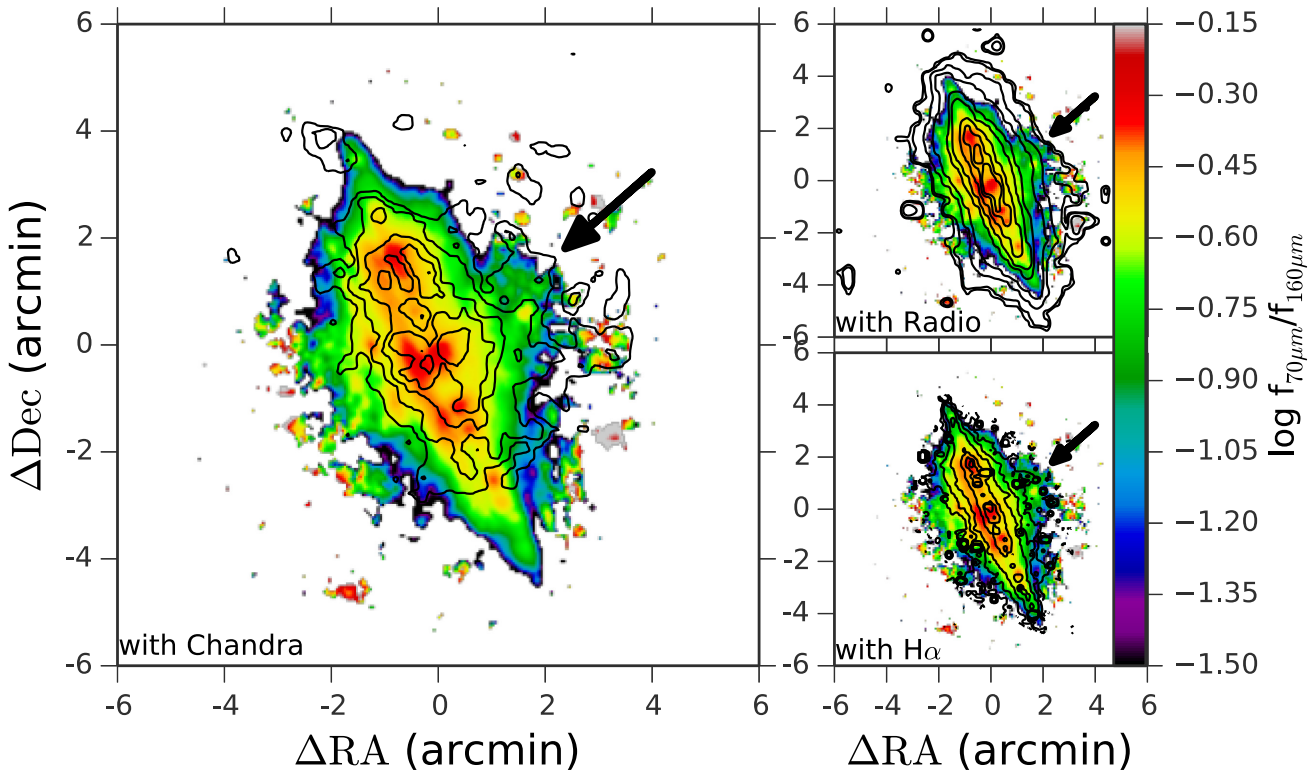


Figure 4. The PACS 70 μm /160 μm colour map. The arrow points at the western superbubble. Left: the X-ray contours for the adaptively smoothed *Chandra* image (0.3–2.0 keV) presented by Hodges-Kluck & Bregman (2012); the contour levels are 9, 10, 15, 20, 30, 40, and 50 counts s^{-1} deg^{-2} . Top right: the same colour maps overlaid with radio continuum contours. The spatial resolution is 17 arcsec \times 12 arcsec and the rms noise is 23 $\mu\text{Jy beam}^{-1}$ (Oosterloo et al. 2007). The contour levels for the radio continuum are 0.1, 0.4, 2, and 10 mJy beam^{-1} . Bottom right: the same colour maps overlaid with $\text{H}\alpha$ surface brightness contours from an $\text{H}\alpha$ image taken at Steward Observatory by C. Engelbracht and calibrated to the total luminosity reported in Hoopes, Walterbos & Rand (1999). Contours are shown at $\Sigma(\text{H}\alpha) = 9.9 \times 10^{-15}$, 1.0×10^{-14} , 1.23×10^{-14} , 2.61×10^{-15} , 6.09×10^{-15} , and 1.02×10^{-13} $\text{erg s}^{-1} \text{cm}^{-2} \text{arcsec}^{-2}$.

would therefore be expected, the radio contours do not describe the PACS colour map well.

The fate of the superbubble will be determined in large part by the CGM. The inner CGM of NGC 891 contains much more cold gas than hot, virialized gas (Hodges-Kluck et al. 2018; Das et al. 2020).

3.3 The dusty halo

On the eastern side of the disc, the 24 μm emission extends 2.03 (5.76 kpc) over most of the disc, reaching a larger distance along the dust spur (Fig. 3). On the western side of the NGC 891 disc, the dusty halo is detected out to 3.68 (10.5 kpc) in the 24 μm map.

The extent of the polycyclic aromatic hydrocarbon emission is similar to that of the cold dust. McCormick et al. (2013) estimate a symmetric extent of ± 5.0 arcmin with a bulk height, $H_{e,\text{PAH}} = 7.1$ kpc.

4 DUST TEMPERATURE AND MASS

We can derive the dust mass, M_d , from the opacity per unit dust mass and the optical depth at FIR wavelengths. We fit a simple, single-temperature modified blackbody (MBB) function to the photometry in the wavelength range $100 \leq \lambda(\mu\text{m}) \leq 500$. The dust spectrum consists of a blackbody spectrum at the dust temperature, $B_\nu(T_d)$, modified by the dust opacity, κ_ν , such that

$$F_\nu = \frac{M_d \kappa_\nu B_\nu(T_d)}{D^2}, \quad (1)$$

where D is the distance to the galaxy. This simple approach yields accurate dust masses and temperatures provided the normalization and the spectral index of the opacity are consistent with full dust models, which include the distribution of dust grain properties and a range of interstellar radiation fields (Bianchi 2013). We adopt a dust opacity model, $\kappa_\nu = \kappa_0(\nu/\nu_0)^\beta$. The normalization, $\kappa_0 = 1.92 \text{ cm}^2 \text{ g}^{-1}$ at 350 μm , and spectral index, $\beta = 2.0$, are based on the Milky Way model presented in Draine et al. (2007).

In the next section, we validate our approach using the SED for the entire galaxy. In Section 4.2, we then describe the dust properties of the morphological components identified in the previous section and defined in Fig. 5. We begin with the dust mass and temperature of each region as a whole, and then we explore these properties on a pixel-by-pixel basis. We estimate dust-to-gas ratios for the various components in Section 4.4.

4.1 Validation of the spectral energy distribution fitting

The top panel of Fig. 6 shows the SED for the entire galaxy. We fit only the 70–500 μm data because the 24 μm flux comes from a warmer dust component. The single-temperature, MBB model with $\beta \equiv 2$ gives a dust mass of $M_d = 1.1 \times 10^8 \text{ M}_\odot$ and dust temperature $T = 21.7 \pm 0.2$ K. We also plot the fit with β taken as a free parameter. A comparison shows that our fitted dust parameters are robust to minor changes in the dust emissivity; see Table 2 for a quantitative comparison.

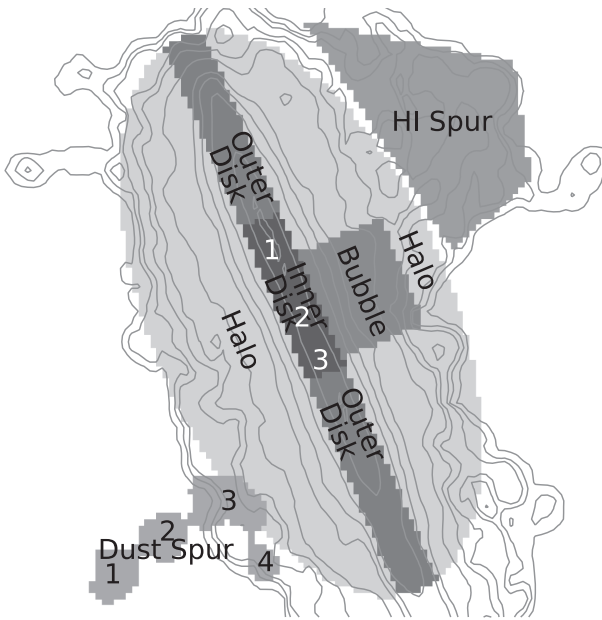


Figure 5. Apertures used for FIR photometry shown relative to H1 21-cm contours from Oosterloo et al. (2007). The semimajor and semiminor axes are 7.4 arcmin (21 kpc) and 3.7 arcmin (10.5 kpc), respectively. We define the thickness of the disc by the thick stellar disc with the width of ± 0.5 arcmin (1.4 kpc). The inner disc has a width of 4.1 arcmin (11.7 kpc) which includes the three star-forming clumps. The other rectangle marks the aperture we use for the superbubble photometry. The height and width of the superbubble are 2.7 arcmin (7.7 kpc) and 2.8 arcmin (8.0 kpc), respectively. The ellipse encompasses the extended halo emission in the lowest resolution band. We define the aperture for the dust spur south-east of the galaxy by the 250 μm contour at $1.7 \text{ mJy pixel}^{-1}$, which is 3σ of the background noise, and outside the extended dust halo. We define an aperture north-west of the galaxy in order to place upper limits on the FIR emission from the H1 spur. Each dust clump and hotspot (star-forming clump) listed in Table 3 is labelled with a number.

The dominant error term is the 10 per cent uncertainty in the flux calibration. To determine the uncertainty on the fitted mass and temperature, we scale the photometry by 10 per cent and refit the models. We find that systematically increasing (or decreasing) all the fluxes can increase (decrease) the fitted dust masses by $\sim 10\text{--}20$ per cent, but dust temperature varies by less than a degree. Our results confirm the dust mass and temperature obtained previously by Hughes et al. (2014) and Bocchio et al. (2016).

The total dust mass fit to the FIR observations is nearly twice that inferred from radiative transfer modeling of the distribution of optical and near-IR emission. For example, when scaled to our adopted distance, Xilouris et al. (1998) found $5.3 \times 10^7 M_\odot$ of dust. A significant fraction of the dust presumably goes undetected because little optical/near-IR radiation emerges from some regions of the galaxy. Previous work has suggested that this hidden dust could reside in a geometrically thinner dust disc (Popescu et al. 2000, 2011) or in clumpy clouds associated with molecular gas (Bianchi 2008). Seon et al. (2014) considered NGC 891 specifically and introduced a thin dust disc of scale height ≈ 5 arcsec to simultaneously describe the distribution of *GALEX* UV emission (Morrissey et al. 2007) and *Herschel* SPIRE photometry (Bianchi & Xilouris 2011).

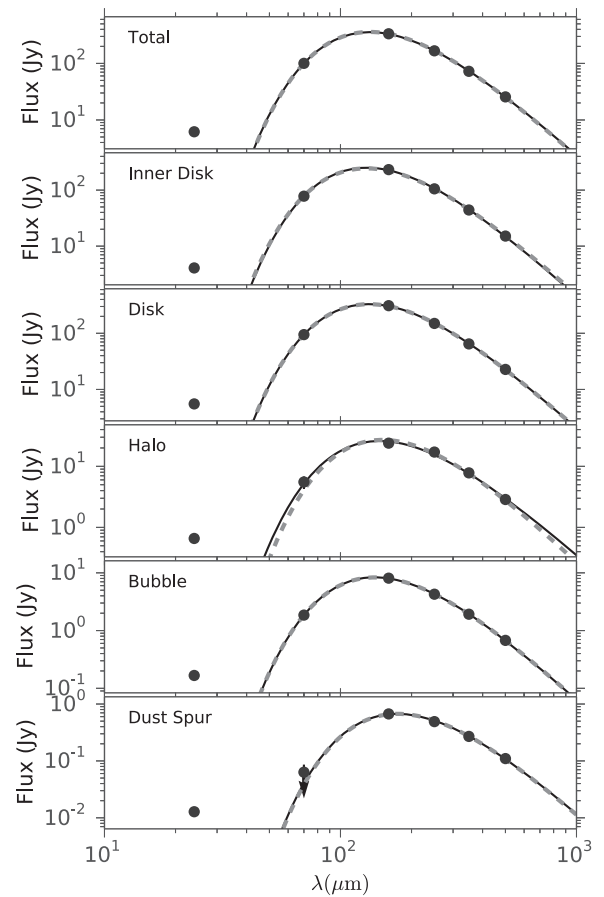


Figure 6. The best-fitting MBB model for integrated flux of each part of NGC 891 in 24, 70, 160, 250, 350, and 500 μm bands. The regions are defined in Fig. 5. The flux for 24 μm is not used for the fitting as it traces different dust components. Grey dashed line is the MBB model fits when β is fixed at 2.

For completeness, we point out that the impact of smaller dust grains (grain radii < 50 \AA) on our fits is constrained by the 24 μm flux. We fit a two temperature model to the full SED including the 24 μm flux. The temperature of a warmer component is not well constrained by this single data point, so we assumed a dust temperature of $T = 220$ K to facilitate comparison to NGC 4631. In Paper I, we found an additional dust component at 220 K in NGC 4631. In their single-temperature, MBB fits, they treated the 70 μm flux as an upper limit because the contribution from the warmer component was non-negligible. We find, however, that the contribution of this warmer component to the 70 μm flux is only 0.3 per cent for this two temperature model fitted to NGC 891. Assuming that the peak wavelength of the MBB curve for the warmer component is shorter than 24 μm , we vary the temperature of the warmer component, and the contribution to 70 μm flux is 1.3 per cent at most. Therefore, we consider 70 μm data point in the same way as other wavelength data in the fitting process. For an assumed warm dust temperature of 220 K, we fit a two-component model and find dust mass in the 220 K component is negligible (~ 0.00003 per cent) compared with dust mass in the ~ 22 K component. The mass in the cool component in this two-component fitting does not deviate from the mass in the one-component, cool component only, fitting as shown in Table 2.

Table 2. Dust properties derived from the MBB model fitting.

Component ^d	Total	Inner disc	Disc	Halo	Superbubble	Dust spur	H I spur
$\log M_{\text{dust}}$	8.025 ± 0.005	7.781 ± 0.012	7.970 ± 0.006	7.163 ± 0.053	6.468 ± 0.003	5.883 ± 0.019	$<3.443^a$
"	8.018 ± 0.007	7.800 ± 0.018	7.970 ± 0.013	7.061 ± 0.074	6.474 ± 0.004	5.868 ± 0.061	...
β	2	2	2	2	2	2	2
"	1.97 ± 0.03	2.09 ± 0.07	2.00 ± 0.05	1.66 ± 0.22	2.03 ± 0.02	1.96 ± 0.16	...
T (K)	21.72 ± 0.05	22.49 ± 0.12	21.89 ± 0.06	19.25 ± 0.62	20.61 ± 0.03	16.57 ± 0.17	19.25^a
"	21.89 ± 0.15	22.02 ± 0.37	21.89 ± 0.26	21.30 ± 1.45	20.50 ± 0.08	16.79 ± 0.81	...
χ^2_v	0.02	0.11	0.03	1.05	0.01	0.08	...
"	0.02	0.09	0.05	0.75	0.01	0.11	...
$\log(M_{\text{HI}}/M_{\odot})^b$	9.64	9.09	9.48	9.10	8.07	<7.22	7.20
$M_{\text{dust}}/M_{\text{gas}}^c$	0.0088	0.0082	0.0095	0.0084	0.025	>0.0046	<0.00017
"	0.0087	0.0086	0.0095	0.0067	0.025	>0.0044	...

Notes: ^aThe dust mass limit is computed by rescaling the MBB model to satisfy the FIR flux limits of the H I spur assuming $\beta = 2$ and the halo dust temperature. ^bThe H I masses were measured from H I map of Oosterloo et al. (2007). ^cThe gas mass was computed as $M_{\text{gas}} = 1.36(M(\text{H}1) + M(\text{H}_2))$, where the coefficient accounts for the gas mass in helium. ^dAlternate rows compare fixed and free spectral indices for the dust opacity.

4.2 SED fitting of dust components

Table 2 summarizes the dust properties for the regions labelled in Fig. 5. The photometry shown in Fig. 6 was obtained after degrading the resolution of the 70, 160, 250, and 350 μm maps to match that of the 500 μm map; see details in Section 2.

Our analysis constrains the contribution from dust well beyond the galactic plane where the starlight is too faint to model its attenuation. Inspection of Table 2 indicates 87 per cent of the dust mass is associated with the galactic disc ($\log(M_{\text{dust}}/M_{\odot}) = 7.970 \pm 0.006$) with 65 per cent of the disc dust concentrated in the inner disc ($\log(M_{\text{dust}}/M_{\odot}) = 7.781 \pm 0.012$). We associate roughly 13 per cent of the total dust mass with the halo component at $|z| > 0.5$, or ± 1.42 kpc; the same halo aperture includes 20 per cent of the total H I mass. This difference can be attributed to the lower dust-to-gas ratio of the halo. Roughly 25 per cent of the halo dust mass ($\log(M_{\text{dust}}/M_{\odot}) = 7.163 \pm 0.053$) comes from the superbubble region, while the dust spur, $\log(M_{\text{dust}}/M_{\odot}) = 5.88 \pm 0.02$, makes a smaller contribution.

The halo dust temperature ($T = 19.24 \pm 0.62$ K) is significantly cooler than the disc dust ($T = 21.89 \pm 0.06$ K). The superbubble dust ($T = 20.61 \pm 0.03$ K) is warmer than the surrounding halo but cooler than the disc. The emission from the dust spur is weak at 70 μm compared to the SPIRE bands, and the fitted dust temperature is considerably lower than that of the disc or halo.

4.3 Pixel-by-pixel analysis

We also examined the variation in dust properties at the resolution limit of the 500 μm image. We fit the SED of all pixels that had $S/N > 3\sigma$ in all five bands, essentially the entire disc component and the disc–halo interface. Hughes et al. (2014) previously found the variation in dust temperature to be more uneven than that of the dust mass. Fig. 7 shows our resulting maps of the temperature and dust surface density, that is, the column density of dust in mass units.

The dust surface density decreases with distance from the nucleus along the major axis. In the vertical direction, the dust surface density drops very quickly to values less than $0.50 M_{\odot} \text{ pc}^{-2}$.

The temperature range in Fig. 8 is similar to the $T_d = 17\text{--}24$ K range found previously by Hughes et al. (2014). The hotspots identified in both the 24 μm map and the 70/160 μm colour map stand out as regions with $T_d \geq 22.5$ K in Fig. 7. This region of the disc is surrounded by a molecular ring (Israel, van der Werf & Tilanus

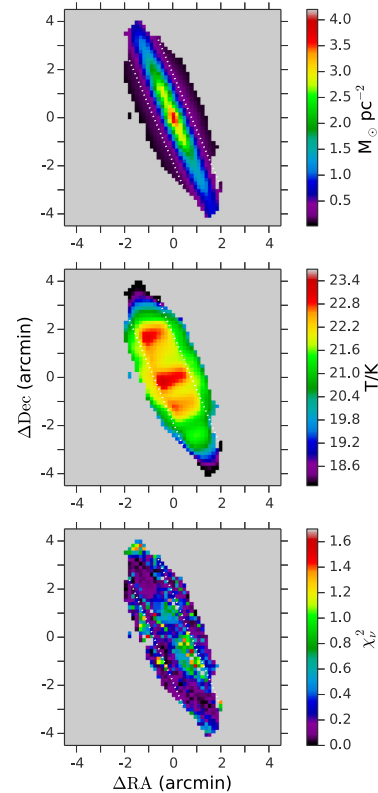


Figure 7. Pixel-to-pixel dust mass, dust temperature, and χ^2_v of the model fit with $\beta = 2$ are shown. Each pixel is $9.0 \text{ arcsec} \times 9.0 \text{ arcsec}$. The disc boundary defined in Fig. 5 is indicated by the white dotted line in each panel.

1999; Scoville et al. 1993). The dust cools off with increasing radius in the disc beyond the molecular ring.

We compare the dust temperature and surface density directly to the 3.6 and 24 μm emission in Fig. 8. The 24 μm emission is a good proxy for the SFRSD (Calzetti et al. 2007), while the 3.6 μm emission traces the stellar mass density. We have colour coded the points in Fig. 8 by their location in NGC 891.

The dust in the mid-plane of the inner disc has temperature, $T_D \approx 22\text{--}23$ K and a high mass column, as indicated by its location in the upper right of Fig. 8. With increasing vertical height at fixed

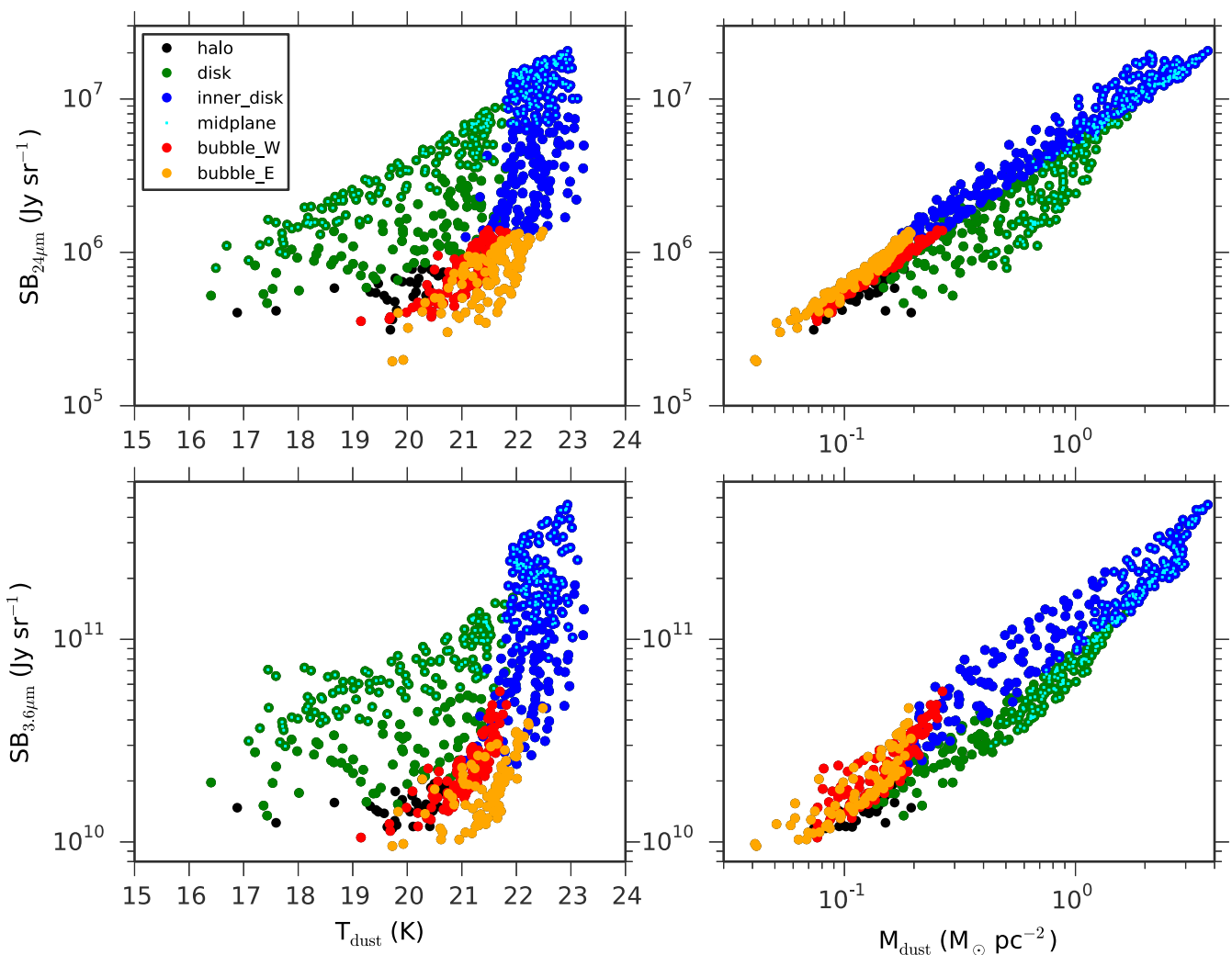


Figure 8. Pixel-to-pixel correlations between dust properties and shorter wavelength emission not used in the SED fitting. The regions shown correspond to the map in Fig. 7. In this plot, *mid-plane* is defined as the region within $|z| \leq 0.7$ arcmin (1.99 kpc) of the disc plane.

radius, the temperature decreases by roughly one degree as the surface brightness drops by an order of magnitude. This locus (blue points) defines a narrow band that continues smoothly into the emission from the superbubble region where the temperature drops a few more degrees (orange and yellow points). Hughes et al. (2014) produced colour maps that identify this same spectral transition with height above the disc. Adding the halo emission immediately above the inner disc extends this correlation to dust temperatures $T_D \lesssim 20$ K. Based on this correlation between dust temperature and 24 μm emission, the dust in and above the inner disc is heated primarily by the starlight from the star-forming regions.

The width of the $\text{SB}(24 \mu\text{m}) - T_D$ locus in the inner disc correlates with radial distance from the nucleus. For example, following the mid-plane points in Fig. 8 from the inner to the outer disc (green points) follows the upper edge of the triangular locus. At fixed 24 μm surface brightness, dust in the mid-plane of the outer disc is cooler than dust above the plane at small radii. Equivalently, at fixed dust temperature, the superbubble and halo emission are not as bright at 24 μm as the outer disc. We expect a transition in the outer disc toward heating by an older stellar population, and it seems plausible this transition manifests as the broad triangle of green points in Fig. 8. Consistent with this interpretation, the 3.6 μm emission from

the mid-plane points in the outer disc (green points with cyan dot) are strongly correlated with the dust temperature. Dust above the mid-plane of the outer disc fills the interior of the triangular locus, as might be expected for dust heated by a mixture of the two stellar populations.

We acknowledge that the temperature correlations look nearly identical against the near-IR (3.6 μm) and mid-IR (24 μm) emission, so the temperatures have the same correlations with the tracers of stellar mass and star formation, respectively. It seems likely that this happens because the mass and SFR both decrease with separation from the centre of the galaxy.

The panels on the right-hand side of Fig. 8 show power law correlations between IR emission and dust surface density. For the inner disc, the correlation is tighter in the mid-IR (24 μm), more closely related to SFRSD. In the outer disc, the 3.6 μm emission shows the stronger correlation, consistent with a closer relation to stellar mass surface density.

4.4 Dust-to-gas ratio

Table 2 compares the dust mass to the gas mass, where all measurements taken from the literature have been scaled to an NGC 891

distance of 9.77 Mpc. The total H I mass of NGC 891 is then $4.4 \times 10^9 M_\odot$ (Oosterloo et al. 2007). The total CO(1–0) intensity (Scoville et al. 1993; Garcia-Burillo et al. 1992) corresponds to a molecular gas mass of $M(\text{H}_2) \approx 4.2 \times 10^9 M_\odot$ for the Bolatto, Wolfire & Leroy (2013) calibration of the CO-to-H₂ conversion factor, $X_{\text{CO}} = 2 \times 10^{20} \text{ cm}^{-2} [\text{K km s}^{-1}]^{-1}$. The ratio of molecular-to-atomic gas is close to unity, $M(\text{H}_2)/M(\text{H I}) \approx 0.95$, which is higher than the median of 0.6 found for Sab galaxies (Obreschkow & Rawlings 2009). Including the mass contribution from helium, the total mass of cold gas is $1.2 \times 10^{10} M_\odot$.

Comparing our measured dust mass to the atomic and molecular gas mass, we find a global gas-to-dust ratio $M_{\text{gas}}/M_{\text{dust}} \approx 110$, where the uncertainty introduced by the X_{CO} -factor is 30 per cent (Bolatto et al. 2013). The gas-to-dust ratios for the SINGS galaxies range from 100 to 340 after scaling the values in table 4 of Draine et al. (2007) to the same X_{CO} and including the helium mass. On this scale, the gas-to-dust ratio of the Milky Way is 200 based on the $M_{\text{dust}}/M_{\text{H}} \approx 0.007$ ratio given by Draine et al. (2007). Based on its atomic and molecular gas content, NGC 891 is dustier than the median Sab galaxy.

The molecular gas is concentrated in the inner disc of NGC 891, so it is not surprising that the inner disc is the dustiest region. The H I disc is larger than the molecular disc. Oosterloo et al. (2007) attribute slightly over 70 per cent of the total H I to the disc, and our measurements of their H I map indicate the inner disc H I mass is $1.22 \times 10^9 M_\odot$, slightly less than half the mass of the entire H I disc. The total gas mass of the inner (and full) disc is then $7.4 \times 10^9 M_\odot$ ($9.8 \times 10^9 M_\odot$). These disc masses do not include the small contribution from warm ionized gas (Rand et al. 1990; Dettmar 1990), but they do include the mass contribution from helium, as described in the notes to Table 2.

The filament north-west of NGC 891 contains at least $1.6 \times 10^7 M_\odot$ of H I (Oosterloo et al. 2007). No thermal dust emission is detected from the H I filament. The upper limit on the dust mass excludes gas-to-dust ratios similar to galactic discs. If the H I filament is accreting gas as Oosterloo et al. (2007) suggest, then the lack of dust emission favours low-metallicity gas. Alternatively, if the H I filament is fountain gas, the time-scale to recycle the disc gas must be long enough to destroy even large grains, which seems unlikely based on the large amount of dust that persists in the CGM (Ménard & Fukugita 2012).

The properties of the dust spur south-east of NGC 891 contrast sharply with those of the H I filament. At the distance of NGC 891, the FIR filament contains nearly $8 \times 10^5 M_\odot$ of dust. Based on the dust mass, this circumgalactic gas was once in a galaxy, either NGC 891 or a satellite. Using the H I map (Oosterloo et al. 2007), the H I mass in the dust spur is less than $2 \times 10^7 M_\odot$. The exceptionally low ratio of neutral hydrogen gas to dust is a puzzle. Perhaps a background source will be found for the IR emission. An alternative, however, is that most of the gas mass is either molecular or ionized.

The mass ratio of H I to dust in the inner CGM of NGC 891 is indistinguishable from the galactic disc. We find this surprising because the neutral fraction of halo gas is around 1 per cent (Popping et al. 2009; Bland-Hawthorn et al. 2017). The dust was presumably made inside galaxies and transported into the halo via outflows or stripping. Gas clouds are normally destroyed by these processes unless special conditions are met, so we would not expect the galactic gas to remain neutral. The inner CGM of NGC 891 contains more neutral gas than the median COS Haloes galaxy (Prochaska et al. 2017; Das et al. 2020). The *disc-like* ratio of H I to dust certainly suggests that the excess of neutral gas in the inner CGM of NGC 891 was removed from galaxies. We will discuss the extrapolated dust mass of the CGM in Section 5.3.

5 DISCUSSION

5.1 The dusty superbubble

We found an extraplanar, dusty region that is significantly warmer than the dusty halo. We called it the dusty superbubble because its location is coincident with thermal X-ray emission ($kT = 0.71 \text{ keV}$) likely associated with an outflow. In Section 5.1.1 below, we show that the thermal energy of this superbubble is sufficient for the superbubble to punch through the disc and blowout into the halo. Blowout in NGC 891 is of particular interest because the SFRSD is a factor of 3 below the commonly assumed threshold of $0.1 M_\odot \text{ yr}^{-1} \text{ kpc}^{-2}$. The fate of this outflow depends largely on the halo gas density profile, which is reasonably well constrained in NGC 891. We present this evolution in Section 5.1.2 and discuss its relationship to the recent detection of cosmic ray advection in the halo of NGC 891.

5.1.1 A galactic wind at SFR surface density $<0.1 M_\odot \text{ yr}^{-1} \text{ kpc}^{-2}$

The first numerical simulations of superbubble blowout predicted that a superbubble would grow to heights of 12 vertical scale heights before the extraplanar shell accelerated and broke up (Mac Low & McCray 1988; Mac Low, McCray & Norman 1989). Given the scale height measurements for NGC 891 (Bocchio et al. 2016), the height of the superbubble (2.7 arcmin) is 8 times the scale height of the dust/gas thick disc (0.34 arcmin in 24 μm) and 68 times that of the dust/gas thin disc (0.04 arcmin in 24 μm).

We will therefore discuss whether the NGC 891 superbubble will develop into a wind. The SFRSD is elevated in the disc of NGC 891, similar to that in a typical disc galaxy several Gyr ago. Whereas the galaxy M82 has become the prototypical starburst outflow, we suggest that the galaxy NGC 891 provides a more typical example of star formation feedback in well-developed galactic discs. To better understand how winds are launched, sophisticated simulations that include multiphase gas, cosmic rays, and turbulence should be tested against the observed properties of NGC 891 as well as starburst galaxies.

The pioneering work of Mac Low & McCray (1988) and Mac Low et al. (1989) predicts that when a superbubble grows to scales comparable to the gas scale height, the expansion velocity $V(r)$ of the shell determines its fate. Shells moving faster than the sound speed of the ambient medium will accelerate as they break through the disc; hydrodynamic instabilities then disrupt the shell, and a free-flowing galactic wind develops (Chevalier & Clegg 1985). Shells with $V(H) \leq c_s$ will continue to decelerate and will eventually collapse due to disruption caused by differential rotation and ISM turbulence. The critical rate of energy injection for blowout to occur depends on the vertical gas density distribution.

Equation (5) of Strickland et al. (2004b) gives the critical power for an exponential gas distribution, $\rho(z) = \rho_0 \exp(-z/H)$, in terms of the gas scale height H . The scale height of the thin, molecular disc in NGC 891 is just 83 pc (Scoville et al. 1993). The H I disc has a thickness $H \approx 2.6 \text{ kpc}$ (Oosterloo et al. 2007), and warm ionized gas extends 4.5 kpc above the disc plane (Dettmar 1990). Scaling to the thick H I disc, the critical mechanical power increases to

$$L_{\text{crit}} = 2.3 \times 10^{39} \text{ erg s}^{-1} \left(\frac{1 \text{ cm}^{-3}}{n_0} \right)^{1/2} \left(\frac{P_0/k}{10^4 \text{ K cm}^{-3}} \right)^{3/2} \times \left(\frac{H}{2.6 \text{ kpc}} \right)^2. \quad (2)$$

Table 3. FIR and radio fluxes within NGC 891.

Part	$\log L_{\text{FIR}}$ (L_{\odot})	$\log L_{60\mu\text{m}}$ (L_{\odot})	$\log L_{\text{Cont}}$ (W Hz^{-1})	q_{IR}	$q_{60\mu\text{m}}$
(1)	(2)	(3)	(4)	(5)	(6)
Total	10.44	9.64	22.00	2.45	2.19
Inner disc	10.30	9.55	21.75	2.56	2.32
Disc	10.41	9.62	21.87	2.55	2.29
Halo	9.28	8.32	21.39	1.90	1.56
Bubble	8.75	7.82	20.81	1.96	1.64
Dust spur	7.60	6.04	19.13	2.48	1.93
Dust spur1	7.23	6.08	18.68	2.56	2.13
Dust spur2	6.91	5.27	17.68	3.24	2.71
Dust spur3	7.12	5.50	18.78	2.35	1.76
Dust spur4	6.56	5.18	18.30	2.27	1.76
Hotspot1	9.76	9.02	21.20	2.57	2.33
Hotspot2	9.80	9.08	21.24	2.57	2.34
Hotspot3	9.56	8.80	20.98	2.59	2.34

Notes: Column (1): part of NGC 891, (2): IR luminosity at 8–1000 μm from SED fit, (3): 60 μm flux computed from the SED fit, (4): radio continuum flux from the continuum map by Oosterloo et al. (2007), (5) $q_{\text{IR}} = \log(\text{IR} / 3.75 \times 10^{12} \text{ W m}^{-2}) - \log(\frac{S_{1.4 \text{ GHz}}}{\text{W m}^{-2} \text{ Hz}^{-1}})$ where IR is the FIR flux and $S_{1.4 \text{ GHz}}$ is flux density at 1.4 GHz. (6): for $q_{60\mu\text{m}}$, the flux at 60 μm is used. This definition is adopted from Condon, Anderson & Helou (1991), Yun et al. (2001), and Bell (2003).

The rate of mechanical power injection from supernovae and stellar winds can be estimated from the SFR. We adopt the solar metallicity models from STARBURST99 and the Salpeter initial mass function. For a star formation history with a constant SFR, the steady-state feedback power is $L_w = 10^{41.8} \text{ erg s}^{-1}$ for an SFR of $1 \text{ M}_{\odot} \text{ yr}^{-1}$ (Leitherer et al. 1999). This calibration includes only stars in the mass range $1 \leq M_{*}/M_{\odot} \leq 100$. To be consistent with the mass range of $0.1 \leq M_{*}/M_{\odot} \leq 100$ used to describe the SFR (Kennicutt 1998), we divide by a factor of 2.55, obtaining $L_w = 10^{41.4} \text{ erg s}^{-1}$ for an SFR of $1 \text{ M}_{\odot} \text{ yr}^{-1}$.

We have listed FIR luminosities for the entire galaxy and the inner disc in Table 3. Applying $\text{SFR}(\text{M}_{\odot} \text{ yr}^{-1}) = 4.5 \times 10^{-44} L_{\text{FIR}}(\text{erg s}^{-1} \text{ Hz}^{-1})$ (Kennicutt 1998), the rate of obscured star formation for the entire galaxy is $4.8 \text{ M}_{\odot} \text{ yr}^{-1}$. This is technically a lower limit on the SFR because not all of the UV light from NGC 891 is obscured by dust. However, we obtained the FUV and NUV magnitudes of NGC 891 from the GALEX nearby galaxy catalog and found that the contribution from unobscured SFR is a relatively small, roughly $0.2 \text{ M}_{\odot} \text{ yr}^{-1}$.

The mechanical energy produced by massive stars in the inner disc is most relevant to the evolution of the superbubble. We measure an inner disc SFR of $3.5 \text{ M}_{\odot} \text{ yr}^{-1}$ from the 24 μm emission. The available mechanical power is then $L_w = 8.7 \times 10^{41} \text{ erg s}^{-1}$, and $L_w/L_{\text{crit}} \approx 380$. Even a few percent of the mechanical energy produced in the inner disc is sufficient to power the expansion of a superbubble that will blowout of the disc of NGC 891.

Theoretical studies have tried to predict the critical SFRSD for the formation of a galactic wind. Overcoming radiative losses has been a major hurdle when star-forming regions are embedded in realistic gas clouds. Murray, Ménard & Thompson (2011) considered the role of radiation pressure from massive star clusters in launching winds and suggested $0.1 \text{ M}_{\odot} \text{ yr}^{-1}$ per kpc^2 as a threshold. Scappapietra (2013) and Hayward & Hopkins (2015) both connected blowout directly to the turbulence in the ISM.

Empirically, Heckman (2002) suggested $0.1 \text{ M}_{\odot} \text{ yr}^{-1}$ per kpc^2 , based largely on nearby starburst galaxies. When they were younger,

however, essentially all disc galaxies drove massive winds (Martin et al. 2012; Rubin et al. 2014). Kornei et al. (2012) measured SFRSDs for redshift $z \sim 1$ star-forming galaxies. Roughly 30 per cent of the outflow galaxies has SFRSDs below the suggested threshold of $0.1 \text{ M}_{\odot} \text{ yr}^{-1}$ per kpc^2 . We suggest that NGC 891 is an excellent nearby analogue, where a wind is developing at an SFRSD a factor of a few lower than the threshold suggested by Heckman (2002). Normalizing the 24 μm luminosity of the inner disc by the area of a disc of diameter 4.1 arcmin, we obtain an SFRSD within the molecular ring of $\Sigma = 0.031 \text{ M}_{\odot} \text{ yr}^{-1} \text{ kpc}^{-2}$ for NGC 891. In comparison, for NGC 4631 (Paper I), the SFRSD is estimated to be $\Sigma = 0.15 \text{ M}_{\odot} \text{ yr}^{-1} \text{ kpc}^{-2}$ as the SFR is $2.9 \text{ M}_{\odot} \text{ yr}^{-1}$ within a radius of 2.5 kpc where almost all of the star formation is taking place, or an SFRSD about 5 times higher than that for NGC 891.

Hayward & Hopkins (2015) describe the condition for blowout by a critical gas fraction, which they find is 30 per cent. We showed in Section 4.4 that the total gas mass of the inner disc is $7.4 \times 10^9 \text{ M}_{\odot}$. We now place bounds on the stellar mass. The IRAC 3.6 μm flux of the inner disc requires $M_* \gtrsim 4 \times 10^{10} \text{ M}_{\odot}$, a lower limit due to optical depth effects. The rotation speed requires a dynamical mass $M_{\text{Dyn}} \approx 6.9 \times 10^{10} \text{ M}_{\odot}$ within a radius of $R = 5.83 \text{ kpc}$. The gas fraction in the inner disc of NGC 891 is in the 10–16 per cent range, a factor of 2 below the Hayward & Hopkins (2015) threshold.

We found that the dusty superbubble is spatially coincident with hot gas ($kT = 0.71 \pm 0.04$ kev) that is concentrated above the star-forming regions in NGC 891 (Hodges-Kluck et al. 2018). This soft X-ray emission very likely comes from the interaction of a hotter wind with cold gas. The cold gas mass is roughly $3 \times 10^8 \text{ M}_{\odot}$ based on the outflowing dust mass, $3 \times 10^6 \text{ M}_{\odot}$, and the disc gas-to-dust ratio. Hot winds have very low emission measure and have only been directly detected in a couple of starburst galaxies (Strickland et al. 2004a, b). It is therefore of significant interest that the central star-forming region in NGC 891 is surrounded by diffuse hard X-ray emission (Hodges-Kluck et al. 2018), possibly related to the hot wind. Regardless of the origin of this hard component, however, NGC 891 shows all the signatures of a thermally driven wind.

5.1.2 Interaction of wind-driven bubble with CGM

As the thermal wind plows into the CGM, it does work on the halo gas and also cools. The classic wind model widely applied to starburst galaxies. Chevalier & Clegg (1985) do not adequately capture this wind–halo interaction because it neglects gravity, radiative losses, and the density profile of the CGM. These processes ultimately determine whether the wind cools, whether a galactic fountain forms, and whether outflowing gas escapes the gravitational potential. Hydrodynamic simulations have not yet spatially resolved the production and evolution of cool gas throughout a galactic disc and the surrounding CGM, but the wind–halo interaction has been explored over a broad parameter range, however, using semi-analytic models (Scappapietra, Ferrara & Madau 2002; Furlanetto & Loeb 2003; Samui, Subramanian & Srianand 2008; Lochhaas et al. 2018). We applied the Lochhaas et al. (2018) model to NGC 891 to gain further insight about the outflow.

The Lochhaas et al. (2018) model extends the classic structure of interstellar bubbles (Weaver et al. 1977) to circumgalactic scales. The hot wind drives an expanding shock front that compresses the surrounding halo gas into a thin shell. A contact discontinuity separates this shell from the wind. The wind fluid is described by the shocked wind immediately behind the shell, an interior region

of unshocked cool wind, and the innermost region of unshocked hot wind. The results suggest that whether adiabatic cooling of the hot wind is accompanied by radiative losses depends on the SFR, halo density profile, and wind density in a non-monotonic manner.

Fig. 2 of Lochhaas et al. (2018) shows the evolution of the contact discontinuity and indicates when the shocked wind begins to cool. The figure cannot be directly applied to NGC 891, however, because the fiducial launch radius, $r_1 = 1$ kpc, corresponds to an SFRSD ≥ 0.3 $M_\odot \text{ yr}^{-1} \text{ kpc}^{-2}$, considerably higher than the 0.031 $M_\odot \text{ yr}^{-1} \text{ kpc}^{-2}$ in the central disc of NGC 891. Repeating the calculation with $r_1 = 7$ kpc and SFR = $4.5 M_\odot \text{ yr}^{-1}$ shows that the NGC 891 outflow lies in a sweet spot where the shocked wind cools radiatively; there is enough mass going into the shocked wind, yet the expansion rate is not fast enough to dropping the density rapidly (Lochhaas, private communication).

After 20 Myr, the contact discontinuity has reached a height of 14 kpc and decelerated to $\approx 200 \text{ km s}^{-1}$. The mean advection speed is therefore larger than the 150 km s^{-1} fit to the spectral index profile of the halo radio emission (Schmidt et al. 2019). Whether this discrepancy is significant is unclear. The semi-analytic model does not specify the physical mechanism launching the wind; it simply predicts how the superbubble evolves for specified α and β . The parameter α describes the efficiency at which supernova energy is transferred to the wind; the β parameter describes the mass loading. Neither parameter is well constrained, and both are assumed to be unity in the Lochhaas et al. (2018) calculations. Values of $\alpha < 1$ would lower the launch velocity, however, so it is not obvious that small adjustments could produce a better match between the velocities.

We have argued that the thermal pressure of the star-forming region is sufficient for blowout, but cosmic ray electrons may also be important for driving the NGC 891 outflow. The non-thermal radio spectral index steepens nearly linearly with height just above the disc of NGC 891, a signature that the cosmic ray electrons are transported by advection rather than diffusion (Mulcahy et al. 2018; Schmidt et al. 2019). The non-thermal spectral index flattens at heights above 2 kpc, consistent with adiabatic expansion dominating synchrotron losses across the region we call the superbubble. Schmidt et al. (2019) argue that the cosmic ray advection plausibly reaches the halo escape velocity 9–17 kpc above the disc.

5.2 The origin of the dust spur and the H I filament

5.2.1 The dust spur

The *Herschel* imaging with PACS and SPIRE confirms the presence of a dust spur discovered in the *Spitzer*/MIPS 24 μm image. The shape of the FIR/submm SED (see Fig. 6) is consistent with emission from a structure associated with NGC 891.

The relative locations of the dust spur to the south-east and the H I spur to the north-west is perplexing in part because these two streams have distinctly different composition. The dust-to-gas ratio (see Table 2) is high in the dust spur but very low in the H I spur. The dust spur is therefore likely composed of higher metallicity gas than the H I spur.

The dust spur contains roughly $7.6 \times 10^5 M_\odot$ of dust. If the dust-to-gas ratio is similar to the disc of NGC 891, then the gas mass is $\approx 9.5 \times 10^7 M_\odot$. This mass exceeds the upper limit on the mass of neutral hydrogen, $M_{\text{H I}} < 1.7 \times 10^7 M_\odot$, in this region of the halo. This apparent contradiction may be explained by additional gas mass in another phase, a higher dust-to-gas ratio in the spur (compared to the NGC 891 disc), or some combination of these properties.

Within the dust spur, the local maxima in the FIR maps coincide with several knots in the radio continuum map. From inspection of Fig. 3, we defined four clumps (see Fig. 5) for which we provide photometry in Table 3. The radio and 60 μm fluxes of these clumps lie on or just above the radio-IR relation defined by star-forming galaxies (de Jong et al. 1985; Condon 1992; Yun et al. 2001). We therefore suggest that the dust spur contains young, possibly obscured, star clusters. Since radio and 60 μm flux both underestimate SFR at low luminosities (Bell 2003), however, it is difficult to make an accurate estimate of their SFR.

Could tidal forces exerted on the disc of NGC 891 by a satellite galaxy produce the dust spur? We estimated the required size of a companion using the Dahari (1984) parameter and the projected separation between the tip of the dust spur and the centre of NGC 891, $S = 7.88$ arcmin. The tidal force on NGC 891 scales as the mass of the companion, $F_t \propto M_c/R^3$, where R is the distance between the galaxies, but the companion mass is unknown. Dahari (1984) introduced a dimensionless parameter $Q \propto F_t$, which uses the diameter of the primary galaxy, $D_p = 14.46$ (de Vaucouleurs et al. 1991), as a scaling parameter, obtaining

$$F_t \propto Q \equiv \frac{(D_c D_p)^{1.5}}{S^3}, \quad (3)$$

and empirically showing that a strong tidal interaction requires $Q \gtrsim 1$. This argument indicates that a satellite galaxy large enough to pull the dust spur out of the NGC 891 disc would have a major axis $D_c \approx 4.30$ or larger. This size is remarkably similar to the extent of the dust spur, which is roughly 2 arcmin by 4 arcmin in Fig. 2. Yet the old stellar population of this hypothetical satellite is not detected.

The dust spur may be the *smoking gun* of a dark satellite passing through the disc of NGC 891. The Milky Way's population of high velocity clouds (HVCs) is thought to include a subpopulation that is confined by dark matter minihaloes (Blitz et al. 1999). The properties of compact, isolated HVCs are similar in many respects to those of dwarf irregular galaxies, but they lack a high surface brightness stellar population (Braun & Burton 2000). They have H I masses of 10^5 – $10^6 M_\odot$, that is, well below the upper limits on the H I mass of the dust spur, but total masses of 10^7 – $10^8 M_\odot$ which are as large as the masses of some dwarf galaxies (Adams, Giovanelli & Haynes 2013). Hydrodynamical simulations of a minihalo colliding with a disc show that the interaction pulls a coherent gas cloud out of the far side of the disc (Nichols et al. 2014; Galyardt & Shelton 2016; Tepper-Garcia & Bland-Hawthorn 2018), a qualitatively different result than the collision of a pure baryonic cloud with a disc. These structures persist for ~ 60 Myr (Galyardt & Shelton 2016) or perhaps even longer (Tepper-Garcia & Bland-Hawthorn 2018), trigger star formation in the minihalo, but eventually deposit the majority of the HVC's gas mass to the disc of the primary galaxy.

5.2.2 The H I filament

Oosterloo et al. (2007) considered several interpretations of the H I spur. They considered gas previously ejected from the disc and now returning to the disc in a galactic fountain and found the recycled gas had to lose significant angular momentum, perhaps to interaction from infall from the intergalactic medium (IGM), to be consistent with the H I kinematics. Alternatively, they suggested the stream could be cold gas directly accreted from the IGM or condensing out of a hot, virialized halo. No star formation has been associated with the H I spur.

In our opinion, the substantial mass of the H I filament, $M(\text{H I}) \approx 1.6 \times 10^7 M_\odot$, suggests a discrete event. We suggest the ram pressure

from the gas halo in NGC 891 pushed the gas out of an HVC or satellite galaxy as it approached the disc. For purposes of illustration, we have estimated the halo density $n_0 \approx 4 \times 10^{-4} \text{ cm}^{-3}$ at $z = 12.5 \text{ kpc}$ and $R = 22.7 \text{ kpc}$ from the fitted H I surface density model (Oosterloo et al. 2007). Models connecting the pressure to the ratio of molecular-to-atomic hydrogen, for example, suggest $P_0/k \lesssim 3 \times 10^3 \text{ cm}^{-3} \text{ K}$ for $\Sigma(\text{H}_2)/\Sigma(\text{H I}) \lesssim 0.5$ (Yim et al. 2011). To strip the ISM from the satellite, the satellite must approach the disc at a velocity

$$V_{\text{sat}} > 210 \text{ km s}^{-1} \left(\frac{P_{\text{sat}}}{3 \times 10^3 \text{ cm}^{-3} \text{ K}} \right)^{1/2} \left(\frac{4 \times 10^{-4} \text{ cm}^{-3}}{n_0} \right)^{1/2} \quad (4)$$

which is comparable to the circular velocity of NGC 891 (Table 1) and therefore a tenable explanation.

5.2.3 Recent accretion

Our analysis suggests that recent accretion events produced both the dust spur and the H I filament, but the nature of these events were different based on the distinct compositions of the two structures. The interaction of an infalling gas-rich satellite or gas stream with the CGM plausibly generated the H I spur, but a collisionless component such as a dark matter minihalo was required to pull the dust spur out the back side of the disc. These processes deliver gas to the disc of NGC 891, thereby fuelling further growth of the stellar disc.

Studies of the stellar halo of NGC 891 show evidence that accretion of satellite galaxies has formed giant streams much like those mapped around the Milky Way (Ibata et al. 2003; Yanny et al. 2003; Belokurov et al. 2007). Mouhcine et al. (2010) resolve structures that loop around the galaxy reaching heights of $\approx 30 \text{ kpc}$ much like the rosette-shaped pattern generated by a tidally disrupting dwarf galaxy. We note that the H I spur follows one of the stellar streams where it plunges toward the disc. This alignment is most easily seen in Fig. 4 of Schulz (2014) who identify seven faint satellites beyond this stellar stream. This satellite population provides more frequent interactions with the disc than the more massive group member UGC 1807 (1:10 mass ratio) over 80 kpc north-west of NGC 891. Interaction with a satellite may also explain the lopsidedness of the disc of NGC 891 (Oosterloo et al. 2007).

5.3 Origins of halo dust

We have detected thermal emission from $1.5 \times 10^7 \text{ M}_\odot$ of cool dust in the inner halo of NGC 891, that is, the region within the ellipse drawn in Fig. 2. We estimate the total halo dust mass from an extrapolation of the halo surface brightness profile. We use the $24 \mu\text{m}$ profile on the west side of the disc and assume the halo extends vertically from a base of radius 20.9 kpc. We equate the central surface brightness of 6.0 MJy sr^{-1} with a mass surface density of $0.20 \text{ M}_\odot \text{ pc}^{-2}$ based on Fig. 7, arriving at a total halo dust mass of $4 \times 10^7 \text{ M}_\odot$.

With this extrapolation, the halo dust mass increases from 15 per cent to roughly 43 per cent of the dust mass in the thick disc. The estimated dust mass in the halo therefore approaches the cosmic ratio of halo dust to disc dust. Ménard & Fukugita (2012) measured the reddening of background quasars caused by dust in Mg II absorbers and found that these absorbers account for most of the dust inside the virial radii of galaxies and that the galaxy haloes contain at least 52 per cent as much dust as do galaxy discs. While we cannot rule out the possibility of substantially more halo dust in a cooler component at $T \sim 7 \text{ K}$, the similarity of these numbers

suggests that the *Herschel* imaging has detected the main component of halo dust in NGC 891.

We have identified two structures, a dusty superbubble and a dust spur, that may pollute the CGM with dust. To add further insight into exactly how dust is transported into the CGM, we applied unsharp masking techniques to highlight the high spatial frequency structure in the dust emission. Regardless of the exact procedure used, the results in Fig. 9 show dust filaments emanating from the hotspots associated with the molecular ring as well as from the central hotspot. These filaments are detected over the full diameter of the molecular ring and extend roughly 4 kpc from the mid-plane. These dust filaments appear to be associated with the feedback processes that are mixing dust into the halo; they are found over a larger region of the disc than the base of the superbubble. It should be possible (in future work) to compare the properties of such filaments directly to wind simulations that take the interactions of the bubbles driven by multiple star-forming regions into account (Tanner, Cecil & Heitsch 2016).

The halo dust clearly traces a fluid that is not pristine gas. While this material most likely originated in galaxies, the question remains whether it was primarily blown out of the disc by feedback processes or whether tidal streams and ram pressure stripping of satellites have contributed a substantial fraction of the mass. The newly discovered dust spur clearly shows that interactions with satellites do play some role. The mass in the dust spur is about 25 per cent of that in the superbubble, however; and the filaments are also lifting dust about 4 kpc off the disc mid-plane. Hence our results favour a dominant role for stellar feedback in enriching the halo with dust.

To determine whether it is energetically plausible for feedback to lift most of the gas associated with the halo dust out of the disc, we conservatively estimate the total mass of gas lifted into the halo along with the dust. The dust-to-gas mass ratio of the galaxy as a whole is $M(\text{dust})/M(\text{gas}) \approx 1/110$. We estimate $M(\text{gas}) \approx 1.7 \times 10^9 \text{ M}_\odot$ just above the disc and, very roughly for the entire halo, $M(\text{gas}) \approx 4 \times 10^9 \text{ M}_\odot$. A lower dust-to-gas ratio would yield more halo gas associated with the dust, but the average galactic value is most appropriate for testing the hypothesis that the dust was lifted out of the disc by feedback. We note that $4 \times 10^9 \text{ M}_\odot$ is a small fraction of the total mass found in the cool CGM of galaxies ($7-12 \times 10^{10} \text{ M}_\odot$, Werk et al. 2014).

Following Hawley & Savage (1997), we assume an isothermal sheet model for the vertical distribution of light and mass in NGC 891. Based on the similarity of the rotation curves for NGC 891 and the Milky Way, we adopt the Milky Way mid-plane mass density ρ_0 (Bahcall 1984) as a proxy for NGC 891; the mass scale height z_0 is taken from IR imaging of NGC 891 (Aoki et al. 1991). The potential energy, W , of a cloud of mass M_{cl} a height z above the mid-plane is then

$$W = 10^{52} \text{ erg} \left(\frac{M_{\text{cl}}}{10^5 \text{ M}_\odot} \right) \left(\frac{z_0}{700 \text{ pc}} \right)^2 \left(\frac{\rho_0}{0.185 \text{ M}_\odot \text{ pc}^{-3}} \right) \times \ln \left[\cosh \left(\frac{z}{z_0} \right) \right]. \quad (5)$$

The energy required to lift the $4 \times 10^9 \text{ M}_\odot$ of H I , H $_2$, and dust in the superbubble to a height of 4.3 kpc is roughly

$$W \approx 1.2 \times 10^{58} \text{ erg} \left(\frac{M_{\text{cl}}}{4 \times 10^9 \text{ M}_\odot} \right) \left(\frac{z_0}{700 \text{ pc}} \right)^2 \times \left(\frac{\rho_0}{0.185 \text{ M}_\odot \text{ pc}^{-3}} \right). \quad (6)$$

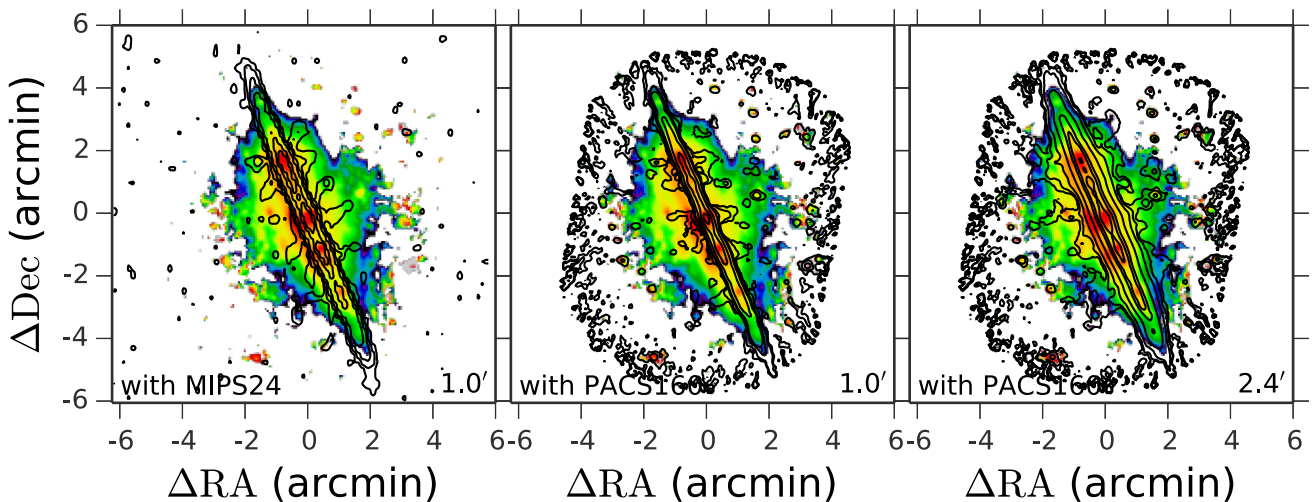


Figure 9. The colour map shown in Fig. 4 is shown with contours of $24 \mu\text{m}$ (left) and $160 \mu\text{m}$ (middle and right) after image sharpening (see the text).

For a constant SFR of $4.8 \text{ M}_\odot \text{ yr}^{-1}$, supernovae and stellar winds provide a mechanical power, $L_w \approx 1.2 \times 10^{42} \text{ erg s}^{-1}$. Assigning an efficiency ϵ for transferring this energy to the cool gas and dust, the time required to enrich the halo with dust is roughly

$$t \approx 3.1 \times 10^8 \epsilon^{-1} \text{ yr.} \quad (7)$$

The current rate of star formation in the disc provides enough feedback energy to lift the dust and associated gas into the halo in just a few rotational periods only if the feedback efficiency is very high. However, if we picture the CGM as continually recycling disc material over a longer time-scale, then feedback can easily account for most of halo dust in NGC 891. For example, if the disc of NGC 891 was assembled at $z \lesssim 2$, and the SFR has steadily declined over the last 10.3 Gyr, then the dust can be lifted into the halo with inefficient feedback characterized by $\epsilon \approx 0.03$.

5.4 Comparison to NGC 4631

It is interesting to compare the feedback in NGC 891 to that in NGC 4631, another edge-on galaxy which we recently studied with *Herschel* in Paper I. The galaxies NGC 4631 and NGC 891 have comparable $\text{H}\alpha$, X-ray, and radio luminosities. Linearly polarized radio continuum emission has been detected in the haloes of both galaxies and shows that magnetic field lines reach into the haloes of both galaxies (Hummel, Beck & Dahlem 1991). The FIR to radio flux ratio for NGC 891 is $q_{60\mu\text{m}} = 2.19$ in Table 3. The FIR luminosity at $60 \mu\text{m}$ is $9.64 - 9.70 \text{ L}_\odot$ (Sanders et al. 2003; Surace, Sanders & Mazzarella 2004) and radio continuum luminosity is $21.85 - 21.76 \text{ W m}^{-2} \text{ Hz}^{-1}$ (Condon, Cotton & Broderick 2002; Murphy et al. 2009). Thus, we estimate $q_{60\mu\text{m}} = 2.03 - 2.19$ for NGC 4631. This ratio is a sensitive probe of age during a starburst phase (Bressan, Silva & Granato 2002), and the comparable values for NGC 4631 and NGC 891 indicate both galaxies are in a post-starburst phase.

In spite of these similarities, the haloes of the two galaxies show some significant differences. The density and scale height of the warm ionized gas are a bit larger in NGC 4631, and the magnetic field extends further into the halo of NGC 4631 (Hummel et al. 1991). The direction of the magnetic field lines is not well constrained for either galaxy due to poorly constrained models for Faraday rotation, but after correction the foreground Faraday rotation the field lines

are quite different in the two galaxies. The magnetic field lines point radially outward from the disc of NGC 4631 while no overall orientation is visible in NGC 891 where the field appears to be drawn into the halo by more local events (especially on the south side of the disc).⁴ Overall, these results suggest the galactic wind is stronger in NGC 4631 than in NGC 891.

Stronger feedback in NGC 4631 would be expected based on its higher SFRSD and gas fraction. The SFRSD of NGC 4631 is about 5 times larger than that of NGC 891 as estimated in Section 5.1. It is also clear that NGC 4631 has a higher gas fraction than NGC 891 based on its higher $\text{H}\alpha$ mass, lower dynamical mass, and later spiral type (de Vaucouleurs et al. 1991).

It is therefore quite interesting to compare the dust properties of these two haloes. We find the measured dust mass of NGC 891 is 2.6 times higher than NGC 4631 in Paper I. We attribute this result to the larger size and mass of NGC 891. The superbubble in NGC 4631 is slightly smaller and contains a factor of 2 less dust mass than the NGC 891 superbubble.

The temperature of the dust, however, differs significantly between the two superbubbles. The temperature of the dusty superbubble is significantly higher in NGC 4631, $T_{\text{dust}} = 24.46 \pm 0.77 \text{ K}$. When we include the $100 \mu\text{m}$ data point from the HEDGES data, the superbubble temperature for NGC 891 increases by $\sim 1 \text{ K}$ which is still 3 K below the the temperature of the superbubble in NGC 4631. When we take the $70 \mu\text{m}$ data point as an upper limit, the temperature decreases slightly. Therefore, the temperature difference of superbubble for NGC 4631 and NGC 891 cannot be alleviated by different SED fitting processes.⁵

⁴The radio continuum emission in Fig. 4 also shows an extension in total intensity away from the disc plane to the south-west (opposite the dust spur). The linear polarization of this south-west extension is larger than the polarization in any other region of NGC 891, and the polarized emission extends further into the halo here than it does above the superbubble (Hummel et al. 1991). Bulk motion has convected the magnetic field outwards, and the adiabatic losses of the electrons may explain the changes in spectral index reported by Hummel et al. (1991). Whether there is a direct connection between this inferred velocity gradient and the dust spur remains unclear.

⁵For the SED modelling, we used five bands, 70, 160, 250, 350, and $500 \mu\text{m}$ while Paper I adopted $100 \mu\text{m}$ in addition to the five bands. Also, in Paper I, the $70 \mu\text{m}$ data point was considered as an upper limit. The higher temperature of the SED fit for NGC 4631 is driven by the data point at $100 \mu\text{m}$. When we

Dust in galaxy haloes can be heated by the evolved stellar population or processes associated with the stellar feedback. Using B - and V -band photometry, Ann, Seo & Baek (2011) measured a scale height for the thick stellar disc of NGC 4631 of 1.33 ± 0.25 and 1.25 ± 0.28 kpc, and Morrison et al. (1997) report an R -band scale height of 1.5–2.5 kpc for NGC 891. It therefore seems unlikely that the stellar halo of NGC 891 is any less effective at heating dust than that in NGC 4631. The SFRSD of NGC 4631 is only slightly higher than that of NGC 891, so an attempt to explain the difference in superbubble temperatures would need to appeal to the lower dust mass and smaller size of the superbubble in NGC 4631. It would be interesting to explore whether these properties of the NGC 4631 superbubble reflect a younger age or the more ordered magnetic field of the halo. The increased temperature of the superbubble might reflect the larger pressure required to push these field lines out of the superbubble’s path.

6 CONCLUSIONS

We present the results of our *Spitzer*/MIPS and *Herschel*/PACS GO observations of NGC 891. The angular resolution and sensitivity allow us to resolve the distribution of dust in the disc and halo. We place these components in the context of the stellar component and multiphase ISM using supplementary observations from the radio to the X-ray. We obtain the following insight into the disc–halo interaction.

(i) The MIPS image at $24 \mu\text{m}$ shows a dust spur extending 20 kpc south-east of the galaxy. The PACS and SPIRE images confirm the presence of this feature. Fitting an MBB model to the SED indicates a dust mass of $7.6 \times 10^5 \text{ M}_\odot$, which is surprisingly large compared to the upper limits on the HI gas mass. The high dust-to-gas ratio is inconsistent with a primordial origin (e.g. a cold stream of infalling material) and indicates the dust was likely pulled out of NGC 891 by a satellite interaction. Its composition differs distinctly from the HI spur to the north-west where we do not detect thermal dust emission. The local maxima in the FIR surface brightness coincide with knots of radio continuum emission, perhaps a sign that they are young star-forming regions. The absence of optical or near-IR emission from the dust spur suggests the colliding satellite had little stellar mass, suggesting that the dust spur may be the remnant of a minihalo collision with the disc.

(ii) The PACS 70/160 μm ratio map draws attention to a superbubble extending over 7 kpc above the mid-plane on its western side. We find a close correspondence between the superbubble and the thermal X-ray emission suggesting that the thermal pressure of hot gas drives the expansion. We argue that the superbubble is likely accelerating as it breaks through the disc because its height exceeds the pressure scale height of not only the thin disc but also the gaseous halo. The feedback associated with the star formation activity within the inner disc appears to be sufficient to launch this galactic wind. The SFRSD of $0.03 \text{ M}_\odot \text{ yr}^{-1} \text{ kpc}^{-2}$ and gas fraction ($\lesssim 10$ per cent) suggest somewhat lower threshold values for driving winds than do the values measured previously in starburst galaxies.

(iii) This disc contains regions of hot dust associated with the galactic centre and the molecular ring. Image sharpening techniques reveal dust filaments rising roughly 4 kpc above these regions. The dust temperature is higher in the inner disc than the halo, and the mass surface density of the dust is centrally concentrated.

include the $100 \mu\text{m}$ data point from the HEDGES data, the temperature of all components of NGC 891 increases by ~ 1 K.

(iv) The halo dust component is detected 10 kpc or more above the entire stellar disc with the measured halo dust mass of $M_{\text{dust, halo}} = 1.5 \times 10^7 \text{ M}_\odot$. A rough extrapolation of the dust mass surface density suggests $\approx 4 \times 10^7 \text{ M}_\odot$ of dust has been lifted into the halo carrying with it a gas mass roughly 100 times larger. This mass flux accounts for roughly 10 per cent of the gas mass estimated to reside in the CGM of similar galaxies.

Because NGC 891 is a very close analogue of the Milky Way in respect to many of its properties, we believe these results provide a viable picture of how dust is deposited in the haloes of typical galaxies. The elevated SFR and molecular gas fraction with respect to the Milky Way would perhaps most closely describe the Milky Way in its recent past when its SFR was higher. In this sense, NGC 891 provides a direct image of the emission from dust and multiphase gas in the inner halo of a galaxy where the baryon budget of the CGM is well-constrained observationally (Hodges-Kluck et al. 2018; Das et al. 2020).

ACKNOWLEDGEMENTS

We thank Cassi Lochhaas for discussions about the circumgalactic bubble which clarified how its structure depends on SFRSD, and we thank an anonymous referee for suggesting we apply the Dahari parameter. This work was supported in part by the National Science Foundation (NSF) under AST-1817125 (CLM) and ASTR1009583 (SV), JPL Awards 1276783 and 1434779, and NASA grants NHSC/JPL RSA 1427277, 1454738 (SV and MM), and ADAP NNX16AF24G (SV). Some of the work was completed at the Aspen Center for Physics, and accompanying support from the NSF through PHY-1066293 is gratefully acknowledged. We deeply regret that the co-author (CE) who provided the $\text{H}\alpha$ image and made a significant contribution to the analysis of the *Spitzer* data did not live to see the article published. *Herschel* is an ESA space observatory with science instruments provided by European-led Principal Investigator consortia and with important participation from NASA.

DATA AVAILABILITY

The data underlying this article will be shared on reasonable request to Dr. Joo Heon Yoon.

REFERENCES

- Adams E. A. K., Giovanelli R., Haynes M. P., 2013, *ApJ*, 768, 77
- Aniano G., Draine B. T., Gordon K. D., Sandstrom K., 2011, *PASP*, 123, 1218
- Ann H. B., Seo M. S., Baek S.-J., 2011, *J. Korean Astron. Soc.*, 44, 23
- Aoki T. E., Hiromoto N., Takami H., Okamura S., 1991, *PASJ*, 43, 755
- Bahcall J. N., 1984, *ApJ*, 276, 169
- Bell E. F. et al., 2008, *ApJ*, 680, 295
- Bell E. F., 2003, *ApJ*, 586, 794
- Belokurov V. et al., 2007, *ApJ*, 654, 897
- Bendo G. J., Galliano F., Madden S. C., 2012, *MNRAS*, 423, 197
- Bianchi S., 2008, *A&A*, 490, 461
- Bianchi S., 2013, *A&A*, 552, A89
- Bianchi S., Xilouris E. M., 2011, *A&A*, 531, L11
- Bland-Hawthorn J., Maloney P. R., Stephens A., Zovaro A., Popping A., 2017, *ApJ*, 849, 51
- Blitz L., Spergel D. N., Teuben P. J., Hartmann D., Burton W. B., 1999, *ApJ*, 514, 818
- Bocchio M., Bianchi S., Hunt L. K., Schneider R., 2016, *A&A*, 586, A8
- Bolatto A. D., Wolfire M., Leroy A. K., 2013, *ARA&A*, 51, 207
- Braun R., Burton W. B., 2000, *A&A*, 354, 853

- Bregman J. N., Pildis R. A., 1994, *ApJ*, 420, 570
- Bressan A., Silva L., Granato G. L., 2002, *A&A*, 392, 377
- Calzetti D. et al., 2007, *ApJ*, 666, 870
- Chevalier R. A., Clegg A. W., 1985, *Nature*, 317, 44
- Condon J. J., 1992, *ARA&A*, 30, 575
- Condon J. J., Anderson M. L., Helou G., 1991, *ApJ*, 376, 95
- Condon J. J., Cotton W. D., Broderick J. J., 2002, *AJ*, 124, 675
- Dahari O., 1984, *AJ*, 89, 966
- Das S., Sardone A., Leroy A. K., Mathur S., Gallagher M., Pingel N. M., Pisano D. J., Heald G., 2020, *ApJ*, 898, 15
- de Jong T., Klein U., Wielebinski R., Wunderlich E., 1985, *A&A*, 147, L6
- de Vaucouleurs G., de Vaucouleurs A., Corwin Herold G. J., Buta R. J., Paturel G., Fouque P., 1991, *Third Reference Catalogue of Bright Galaxies*, Springer, New York, NY
- Dettmar R.-J., 1990, *A&A*, 232, L15
- Draine B. T. et al., 2007, *ApJ*, 663, 866
- Engelbracht C. W. et al., 2007, *PASP*, 119, 994
- Ferrarese L. et al., 2000, *ApJ*, 529, 745
- Furlanetto S. R., Loeb A., 2003, *ApJ*, 588, 18
- Galyardt J., Shelton R. L., 2016, *ApJ*, 816, L18
- Garcia-Burillo S., Guelin M., Cernicharo J., Dahlem M., 1992, *A&A*, 266, 21
- Gordon K. D. et al., 2005, *PASP*, 117, 503
- Griffin M. J. et al., 2010, *A&A*, 518, L3
- Hayward C. C., Hopkins P. F., 2015, preprint ([arXiv:1510.05650](https://arxiv.org/abs/1510.05650))
- Heckman T. M., 2002, in Mulchaey J. S., Stocke J. T., eds, *ASP Conf. Ser. Vol. 254, Extragalactic Gas at Low Redshift*, Astron. Soc. Pac., San Francisco, p. 292, preprint ([astro-ph/0107438](https://arxiv.org/abs/astro-ph/0107438))
- Hodges-Kluck E. J., Bregman J. N., 2012, *ApJ*, 762, 12
- Hodges-Kluck E. J., Bregman J. N., Li J.-t., 2018, *ApJ*, 866, 126
- Hoopes C. G., Walterbos R. A. M., Rand R. J., 1999, *ApJ*, 522, 669
- Howk J. C., Savage B. D., 1997, *AJ*, 114, 2463
- Howk J. C., Savage B. D., 2000, *AJ*, 119, 644
- Hughes T. M. et al., 2014, *A&A*, 565, A4
- Hummel E., Beck R., Dahlem M., 1991, *A&A*, 248, 23
- Ibata R. A., Irwin M. J., Lewis G. F., Ferguson A. M. N., Tanvir N., 2003, *MNRAS*, 340, L21
- Ibata R., Mouhcine M., Rejkuba M., 2009, *MNRAS*, 395, 126
- Israel F. P., van der Werf P. P., Tilanus R. P. J., 1999, *A&A*, 344, L83
- Kennicutt R. C., Jr, 1998, *ARA&A*, 36, 189
- Kornei K. A., Shapley A. E., Martin C. L., Coil A. L., Lotz J. M., Schiminovich D., Bundy K., Noeske K. G., 2012, *ApJ*, 758, 135
- Leitherer C. et al., 1999, *ApJS*, 123, 3
- Lochhaas C., Thompson T. A., Quataert E., Weinberg D. H., 2018, *MNRAS*, 481, 1873
- Mac Low M.-M., McCray R., 1988, *ApJ*, 324, 776
- Mac Low M.-M., McCray R., Norman M. L., 1989, *ApJ*, 337, 141
- Martin C. L., Shapley A. E., Coil A. L., Kornei K. A., Bundy K., Weiner B. J., Noeske K. G., Schiminovich D., 2012, *ApJ*, 760, 127
- McCormick A. et al., 2018, *MNRAS*, 477, 699
- McCormick A., Veilleux S., Rupke D. S. N., 2013, *ApJ*, 774, 126
- Meléndez M. et al., 2015, *ApJ*, 804, 46 (M15)
- Ménard B., Fukugita M., 2012, *ApJ*, 754, 116
- Morrison H. L., Miller E. D., Harding P., Stinebring D. R., Boroson T. A., 1997, *AJ*, 113, 2061
- Morrissey P. et al., 2007, *ApJS*, 173, 682
- Mouhcine M., Ibata R., Rejkuba M., 2010, *ApJ*, 714, L12
- Mulcahy D. D. et al., 2018, *A&A*, 615, A98
- Murphy E., 2011, Herschel Space Observatory Proposal, pid. 1658, available at: <https://ui.adsabs.harvard.edu/abs/2011hers.prop.1658M/abstract>
- Murphy E. J., Kenney J. D. P., Helou G., Chung A., Howell J. H., 2009, *ApJ*, 694, 1435
- Murray N., Ménard B., Thompson T. A., 2011, *ApJ*, 735, 66
- Nichols M., Mirabal N., Agertz O., Lockman F. J., Bland-Hawthorn J., 2014, *MNRAS*, 442, 2883
- Obreschkow D., Rawlings S., 2009, *MNRAS*, 394, 1857
- Oosterloo T., Fraternali F., Sancisi R., 2007, *AJ*, 134, 1019
- Ott S., 2010, *ASP Conf. Ser. Vol. 434, Galaxy Wars: Stellar Populations and Star Formation in Interacting Galaxies*, Astron. Soc. Pac., San Francisco, p. 9
- Pingel N. M. et al., 2018, *ApJ*, 865, 36
- Poglitsch A. et al., 2010, *A&A*, 518, L2
- Popescu C. C., Misiriotis A., Kylafis N. D., Tuffs R. J., Fischera J., 2000, *A&A*, 362, 138
- Popescu C. C., Tuffs R. J., Dopita M. A., Fischera J., Kylafis N. D., Madore B. F., 2011, *A&A*, 527, A109
- Popping A., Davé R., Braun R., Oppenheimer B. D., 2009, *A&A*, 504, 15
- Prochaska J. X. et al., 2017, *ApJ*, 837, 169
- Rand R. J., Kulkarni S. R., Hester J. J., 1990, *ApJ*, 352, L1
- Reach W. T. et al., 2005, *PASP*, 117, 978
- Reynolds R. J., 1989, *ApJ*, 339, L29
- Rieke G. H. et al., 2004, *ApJS*, 154, 25
- Roussel H., 2013, *PASP*, 125, 1126
- Rubin K. H. R., Prochaska J. X., Koo D. C., Phillips A. C., Martin C. L., Winstrom L. O., 2014, *ApJ*, 794, 156
- Samui S., Subramanian K., Srianand R., 2008, *MNRAS*, 385, 783
- Sanders D. B., Mazzarella J. M., Kim D.-C., Surace J. A., Soifer B. T., 2003, *AJ*, 126, 1607
- Scannapieco E., 2013, *ApJ*, 763, L31
- Scannapieco E., Ferrara A., Madau P., 2002, *ApJ*, 574, 590
- Schmidt P. et al., 2019, *A&A*, 632, A12
- Schulz E., 2014, *ApJ*, 790, 76
- Scoville N. Z., Thakkar D., Carlstrom J. E., Sargent A. I., 1993, *ApJ*, 404, L59
- Seon K.-I., Witt A. N., Shinn J.-H., Kim I.-J., 2014, *ApJ*, 785, L18
- Strickland D. K., Heckman T. M., Colbert E. J. M., Hoopes C. G., Weaver K. A., 2004a, *ApJS*, 151, 193
- Strickland D. K., Heckman T. M., Colbert E. J. M., Hoopes C. G., Weaver K. A., 2004b, *ApJ*, 606, 829
- Surace J. A., Sanders D. B., Mazzarella J. M., 2004, *AJ*, 127, 3235
- Swaters R. A., Sancisi R., van der Hulst J. M., 1997, *ApJ*, 491, 140
- Tanner R., Cecil G., Heitsch F., 2016, *ApJ*, 821, 7
- Tepper-Garcia T., Bland-Hawthorn J., 2018, *MNRAS*, 473, 5514
- Tüllmann R., Pietsch W., Rossa J., Breitschwerdt D., Dettmar R.-J., 2006, *A&A*, 448, 43
- Tumlinson J. et al., 2011, *Science*, 334, 948
- van der Kruit P. C., Searle L., 1981, *A&A*, 95, 116
- Veilleux S., Maiolino R., Bolatto A. D., Aalto S., 2020, *A&AR*, 28, 2
- Weaver R., McCray R., Castor J., Shapiro P., Moore R., 1977, *ApJ*, 218, 377
- Werk J. K. et al., 2014, *ApJ*, 792, 8
- Xilouris E. M., Alton P. B., Davies J. I., Kylafis N. D., Papamastorakis J., Trehewella M., 1998, *A&A*, 331, 894
- Yanny B. et al., 2003, *ApJ*, 588, 824
- Yim K., Wong T., Howk J. C., van der Hulst J. M., 2011, *AJ*, 141, 48
- Yun M. S., Reddy N. A., Condon J. J., 2001, *ApJ*, 554, 803
- Zibetti S., 2009, preprint ([arXiv:0911.4956](https://arxiv.org/abs/0911.4956))